

1 **Reduced Arctic sea ice extent during the mid-Pliocene Warm Period**  
2 **concurrent with increased Atlantic-climate regime**

3  
4 \*Waliur Rahaman<sup>1</sup>, Lukas Smik<sup>2</sup>, Deniz Köseoğlu<sup>3</sup>, Lathika N<sup>1</sup>, Mohd  
5 Tarique<sup>1,4</sup>, Meloth Thamban<sup>1</sup>, Alan Haywood<sup>5</sup>, Simon T. Belt<sup>2</sup>, J. Knies<sup>3,6</sup>

6  
7 <sup>1</sup> National Centre for Polar and Ocean Research (NCPOR), Ministry of  
8 Earth Sciences, Vasco-da-Gama, Goa 403804, India

9 <sup>2</sup>School of Geography, Earth and Environmental Sciences, University of  
10 Plymouth, PL4 8AA, UK

11 <sup>3</sup>CAGE – Centre for Arctic Gas Hydrate, Environment and Climate,  
12 Department of Geosciences, UiT The Arctic University of Norway, 9037  
13 Tromsø, Norway

14 <sup>4</sup>Department of Marine Geology, Mangalore University, Mangalore, India

15 <sup>5</sup>School of Earth and Environment, University of Leeds, Woodhouse Lane,  
16 Leeds, LS2 9JT, UK

17 <sup>6</sup>Geological Survey of Norway, N-7491 Trondheim, Norway

18  
19  
20 **Revised submission to Earth and Planetary Science Letter (EPSL)**

21 \*Corresponding author ([waliur@ncpor.res.in](mailto:waliur@ncpor.res.in))

22 Orchid ID: <https://orcid.org/0000-0001-6439-4529>

25 **Abstract**

26 Quantifying the contribution of poleward oceanic heat transport to the Arctic Ocean is  
27 important for making future sea ice and climate predictions. To highlight its potential  
28 importance in a warmer world, we present a new record of water-mass exchange  
29 between the Atlantic and the Arctic Oceans using the authigenic neodymium isotopic  
30 composition of marine sediments from the Fram Strait during the past ~3.4 to 2.6 Ma. In  
31 this study, we target the mid-Pliocene Warm Period (mPWP: 3.264–3.025 Ma) of the  
32 Pliocene epoch, the most recent geological analogue for future climate change. We  
33 complement our semi-quantitative water mass exchange reconstruction with estimates  
34 of spring sea ice concentration based on source-specific biomarkers. Our estimates of  
35 volume transport of warm waters into the Arctic Ocean suggest long-term secular  
36 changes from the lowest during the Marine Isotope Stage M2 “glacial” (3.312–3.264  
37 Ma), to near complete “Atlantification” of the Eurasian sector of the Arctic Ocean during  
38 the mPWP. Orbital forcing is found to be the dominant controlling factor for modulating  
39 northward volume transport of Atlantic-derived water masses, with an associated  
40 reduction in Arctic spring sea ice concentration of ~30-35%. Current generation models  
41 often produce diverging results, however, and have not yet been validated against proxy  
42 data in northern high latitude settings during the mPWP. Our new results of northward  
43 volume transport and sea ice extent therefore provide much needed input for validation  
44 of current generation models aimed at improving the robustness of future climate  
45 modelling in the Arctic.

46 **Keywords: mid-Pliocene, North Atlantic Current, Arctic, Sea ice, Atlantification**

## 47 **1. Introduction**

48 The most dramatic changes observed in the Arctic Ocean during the recent past are the  
49 unprecedented reductions in sea ice extent and thickness (Kinnard et al., 2011).  
50 Although coupled ice-ocean model simulations suggest that the recent warming in the  
51 Northern Hemisphere is responsible for this decline (Petrie et al., 2015), there is  
52 disagreement between data and models over the impact of atmospheric warming  
53 versus oceanic heat transport on sea ice decline (Ding et al., 2018; Dowsett et al., 2012;  
54 Haywood et al., 2013). Studies based on proxy reconstructions of heat and volume  
55 transport through the Fram Strait (Spielhagen et al., 2011), and in-situ observations in  
56 the eastern Arctic Ocean (Polyakov et al., 2017), suggest that enhanced oceanic heat  
57 transport by the North Atlantic Current (NAC) over the past few decades likely explains  
58 the weakened stratification, increased vertical mixing and reduced sea ice in the Atlantic  
59 sector of the Arctic, collectively termed “Atlantification” (Polyakov et al., 2017;  
60 Spielhagen et al., 2011). In order to improve our understanding about Arctic sea ice  
61 variability, particularly within the current context of rapid global warming, it is imperative  
62 to reconstruct sea ice conditions during previous warm climate states, and decipher the  
63 underlying mechanisms that control its distribution. One such period in Earth’s history is  
64 the Pliocene (5.33–2.58 Ma), which experienced higher global temperatures than pre-  
65 industrial (Dowsett et al., 2009), and was characterized by a gradual transition from  
66 relatively warm climates during the Early Pliocene towards cooler conditions in the Late  
67 Pliocene. Some previous organic geochemical-based proxy climate reconstructions for  
68 the Pliocene have been conducted for the North Atlantic and Fram Strait (Clotten et al.,  
69 2018; Knies et al., 2002), and similar studies have been carried out for other warm

70 interglacials such as the Eemian (Marine Isotope Stage (MIS) 5e) and the early  
71 Holocene (Belt et al., 2015; Müller et al., 2012; Stein et al., 2017). However, the roles of  
72 atmospheric warming versus northward heat transport in controlling sea ice conditions  
73 were not assessed as part of these studies.

74         Here we aimed to identify the potential impact of future changes in oceanic heat  
75 transport into the Arctic Ocean and the effects of “Atlantification” in a warmer than  
76 modern climate. To achieve this, we conducted a semi-quantitative assessment of  
77 northward volume transport of Atlantic water through the Fram Strait during a geological  
78 period when (1) climatic conditions in terms of temperature and atmospheric CO<sub>2</sub> level  
79 were analogous to modern/or future projected scenarios and (2) global oceanographic  
80 and tectonic settings were nearly identical to today. The mid-Pliocene Warm Period  
81 (mPWP: 3.264–3.025 Ma) is known to be warmer (globally) than today (Dowsett et al.,  
82 1992; Haywood et al., 2016), with atmospheric CO<sub>2</sub> concentrations estimated to be in  
83 the range 350-450 ppmv (Berends et al., 2019; Foster et al., 2017). Hence, the mPWP  
84 has been proposed as a possible reference for future warm climate states (IPCC, 2013).  
85 Confirmation of increased polar ocean heat transport and reduced sea ice in the Arctic  
86 Ocean during the mPWP (Raymo et al., 1996) would therefore be of clear benefit for the  
87 assessment of coupled ocean-ice-atmosphere model simulations of the mPWP  
88 (Haywood et al., 2016).

89         To achieve this objective, we first reconstructed an orbital-resolution record of  
90 watermass mixing between the NAC and Arctic-derived polar waters (PW) in the Fram  
91 Strait (Fig. 1), based on authigenic neodymium (Nd) isotopes ( $\epsilon_{Nd}$ ). The radiogenic  
92 isotope composition of Nd in seawater reveals changes in watermass mixing and

93 circulation patterns due to its quasi-conservative behavior (Martin, 2002) and lower  
94 average oceanic residence time (360–2000 years) compared to the global ocean mixing  
95 time ~1500 years (Tachikawa et al., 1999) . Critically, in contrast to stable oxygen ( $\delta^{18}\text{O}$ )  
96 or carbon isotope ( $\delta^{13}\text{C}$ ) measurements, the Nd isotope ratios are not affected by  
97 isotopic fractionation resulting from any biological or other low-temperature processes,  
98 so represent a robust proxy for paleo-water mass circulation (Martin, 2002). In a modern  
99 context, the majority of Atlantic-derived water masses are transported northward into  
100 the Arctic Ocean along the Svalbard continental margin, which is the northernmost  
101 extension of the NAC (Fig. 1). This warm water submerges into the Arctic Ocean or is  
102 deflected westward and submerged southward below cold and less saline waters of the  
103 East Greenland Current (EGC). All of these modern water masses possess  
104 characteristic Nd isotope signatures (Fig. 1) (Laukert et al., 2017; Werner et al., 2014).  
105 Less radiogenic values are indicative of a stronger influence of NAC flowing into the  
106 Nordic Seas (present-day  $\epsilon_{\text{Nd}} = -13.2$  to  $-13.0$ ) (Teschner et al., 2016) while more  
107 radiogenic Nd isotope signatures reflect enhanced contribution from Arctic-derived polar  
108 waters (PW) (Laukert et al., 2017) (e.g.  $\epsilon_{\text{Nd}} = -9.9$ ). For this study, an orbital-resolution  
109 (~5 ka) authigenic  $\epsilon_{\text{Nd}}$  record was obtained through analysis of bulk sediments from  
110 Ocean Drilling Program (ODP) Hole 910C (hereafter referred to 910C) on the Yermak  
111 Plateau, eastern Fram Strait, ( $80^{\circ}15.894'\text{N}$ ,  $6^{\circ}35.430'\text{E}$ , water depth: 556.4 m) covering  
112 the interval between 3.4 Ma and 2.6 Ma. This new record is supplemented by a  
113 previously published low-resolution (60-70 ka) record of authigenic  $\epsilon_{\text{Nd}}$  from ODP Hole  
114 911A ( $80^{\circ} 28.466' \text{ N}$ ,  $8^{\circ} 13.640' \text{ E}$ , water depth: 902 m) (hereafter referred to 911A) at  
115 the eastern flank of the Yermak Plateau (Teschner et al., 2016).

116 To identify the corresponding changes in sea ice coverage and carbonate  
117 chemistry, the sea ice biomarker proxy  $IP_{25}$ , a related open-water highly branched  
118 isoprenoid (HBI) lipid (HBI III), and calcium carbonate ( $CaCO_3$ ) abundance related to  
119 carbonate chemistry and productivity/or preservation, were also analyzed. Over the last  
120 decade, source-specific highly branched isoprenoid (HBI) lipid biomarkers have  
121 emerged as reliable proxies for reconstructing past sea ice extent in the polar oceans  
122 (Belt, 2018 and references therein). The most frequently studied biomarker is the mono-  
123 unsaturated HBI  $IP_{25}$ , first identified in Arctic sea ice and sediments by Belt et al. (2007),  
124 and has since been used as a binary measure of seasonal Arctic sea ice in the past for  
125 time scales ranging from recent decades to several millions of years. Further, by  
126 combining sedimentary  $IP_{25}$  concentrations with those of various phytoplankton  
127 biomarkers in the form of the  $IP_{25}$ -phytoplankton ( $PIP_{25}$ ) index, semi-quantitative  
128 estimates of sea ice extent can be achieved (Belt, 2018; Müller et al., 2011). Finally,  
129 when a further tri-unsaturated HBI (often referred to as HBI III; Belt et al., 2015) is used  
130 as the open water counterpart to  $IP_{25}$ , the resulting  $PIP_{25}$  index (i.e.  $P_{III}IP_{25}$ ) exhibits a  
131 reasonably good linear relationship to spring sea ice concentration (%SpSIC) for the  
132 Barents Sea and neighboring regions (Smik et al., 2016).

133 North Atlantic and Arctic waters are characterized by distinct carbonate  
134 characteristics (e.g. alkalinity and pH), so carbonate abundance in sediments from the  
135 Fram Strait (mixing zone) can be used to infer changes in carbonate chemistry,  
136 productivity, preservation and dissolution resulting from variable paleo-oceanographic  
137 changes. For example, warm and carbonate-rich North Atlantic waters lead to better  
138 preservation compared to cold carbonate depleted Arctic waters. However, one of the

139 caveats attached with the application is the input of detrital carbonate to the core site.  
140 Study of carbonates in the core sites ODP 909 (Fram Strait) and 911 (Yermak Plateau)  
141 have suggested that predominant fractions of the carbonate abundance in the  
142 sediments are of authigenic origin and therefore controlled carbonate abundance  
143 variability in the Fram-Strait (Chow et al., 1996). Further, in previous studies, therefore,  
144 high carbonate preservation in sediments from the Fram Strait has been attributed to  
145 increased influence of Atlantic water masses (Zamelczyk et al., 2014). In the  
146 Norwegian–Greenland Sea, high carbonate content has also been interpreted to reflect  
147 the influence of warm Atlantic water masses, while low carbonate content were  
148 attributed to cold surface waters (Huber et al., 2000). Therefore, a combined authigenic  
149 Nd isotope and carbonate record from the Fram-Strait were employed in the present  
150 study to reconstruct northward volume and heat transport by the NAC.

151

## 152 **2. Material and methods**

153 Sediments of ODP Hole 910C (80°15.894' N, 6°35.430' E; water depth: 556.4 m)  
154 have been analyzed in this study. The deep-water Nd isotope signal was extracted from  
155 the Fe-Mn oxyhydroxide fraction of bulk sediment following the leaching procedure  
156 described below. Further details of Nd isotopes, HBI biomarkers and calcium carbonate  
157 abundance measurements are given in the following sections.

### 158 **2.1 Neodymium isotope analysis in authigenic fractions**

159 We measured the neodymium (Nd) isotope composition in authigenic phases extracted  
160 from the bulk sediments of 910C. This new record of authigenic  $\epsilon_{Nd}$  is supplemented by  
161 an earlier published low-resolution (60-70 ka) record from ODP Hole 911A at the

162 eastern flank of the Yermak Plateau (Teschner et al., 2016). Therefore, for comparison,  
163 and to avoid discrepancies related to the analytical methods for the extraction of  
164 authigenic Nd from sediments and its isotope measurements, we adopted the same  
165 method of Teschner et al. (2016). The procedure thus began with extracting the past  
166 seawater signal contained in the diagenetic coatings from ~2 g of sample material with a  
167 0.05 M hydroxylamine hydrochloride and 15% acetic acid solution (HH leach), buffered  
168 to a pH of ~3.5 to 4.0, without rinsing before the HH leach. The rare earth elements  
169 (REEs) in the solution were separated using cation exchange columns filled with  
170 AG50WX8 resin (mesh 200–400). Nd was separated from the other REEs using  
171 columns filled with Ln-Spec resin (50–100 mesh). Nd isotopes were analyzed using a  
172 multi-collector inductively coupled plasma mass spectrometer (MC-ICP-MS, Thermo  
173 Scientific Neptune Plus) at the National Centre for Polar & Ocean Research (NCPOR),  
174 Goa, India. All Nd isotope ratios ( $^{143}\text{Nd}/^{144}\text{Nd}$ ) presented here were corrected for mass  
175 bias following an exponential law using the known value of  $^{146}\text{Nd}/^{144}\text{Nd}$  of 0.7219. The  
176 instrument bias was normalized to the accepted  $^{143}\text{Nd}/^{144}\text{Nd}$  value of the JNdi-1  
177 standard of 0.512115 (Tanaka et al., 2000). Repeat measurements of the JNdi-1  
178 standard yielded a long-term average reproducibility of  $\pm 0.3 \epsilon_{\text{Nd}}$  ( $2\sigma$ ;  $n = 103$ ) over a  
179 period of nine months. Average procedural blank ascertained for Nd ( $n = 4$ ) was 170 pg  
180 which is less than 1% of the total Nd analyzed in samples, so blank correction was not  
181 applied. All Nd isotope ratios are reported in epsilon notation according to Equation 1.

$$182 \quad \epsilon_{\text{Nd}} = \left[ \frac{^{143}\text{Nd}/^{144}\text{Nd}_{\text{sample}}}{^{143}\text{Nd}/^{144}\text{Nd}_{\text{CHUR}}} - 1 \right] \times 10^4 \quad \text{Eq (1)}$$

183 In order to check the quality of the authigenic Nd isotope analyses, which includes  
184 chemical extractions of the authigenic Nd and its isotopic measurements, we analyzed a



185 total of 16 replicates. Data from these replicates (with a variable range of  $\epsilon_{\text{Nd}}$ ) are highly  
186 consistent (Supplementary Fig. S1); most of them are falling on the equiline (1:1 line).

## 187 **2.2 HBI biomarkers**

188 The HBI biomarkers IP<sub>25</sub> and HBI III were extracted from freeze-dried  
189 subsamples (~2–4 g) from 910C. Samples were saponified in a methanolic KOH  
190 solution (~5 mL H<sub>2</sub>O: MeOH (1:9); 5% KOH) for 60 min (70 °C). Hexane (3×2 mL) was  
191 added to the saponified content, with supernatant solutions, containing non-saponifiable  
192 lipids (NSLs), transferred with glass pipettes to clean vials and dried over a gentle  
193 stream of N<sub>2</sub> to remove traces of H<sub>2</sub>O/MeOH. NSLs were then re-suspended in hexane  
194 (0.5 mL) and fractionated using column chromatography (SiO<sub>2</sub>; 0.5 g). Non-polar lipids,  
195 including IP<sub>25</sub> and HBI III, were eluted with hexane (6 mL). Each non-polar fraction was  
196 further purified to remove saturated components using silver-ion chromatography (Belt  
197 et al., 2015) with saturated compounds eluted with hexane (2 mL) and unsaturated  
198 compounds, including HBIs, collected in a subsequent acetone fraction (3 mL). Prior to  
199 extraction, samples were spiked with an internal standard (9-octylheptadec-8-ene, 9-  
200 OHD, 10  $\mu\text{L}$ ; 10  $\mu\text{g mL}^{-1}$ ) to permit quantification of HBIs. Analysis of fractions  
201 containing IP<sub>25</sub> and HBI III was carried out using gas chromatography–mass  
202 spectrometry (GC–MS) following the methods and operating conditions described  
203 elsewhere (Belt et al., 2012). Mass spectrometric analysis was carried out in total ion  
204 current (TIC) and selected ion monitoring (SIM) modes. The identification of IP<sub>25</sub> and  
205 other HBIs was based on their characteristic GC retention indices (e.g. RI<sub>HP5MS</sub> = 2081  
206 and 2044 for IP<sub>25</sub> and HBI III, respectively) and mass spectra (Belt, 2018).  
207 Quantification of all HBIs was achieved by comparison of mass spectral responses of

208 selected ions (e.g.  $IP_{25}$ ,  $m/z$  350; HBI III,  $m/z$  346) in SIM mode with those of the internal  
209 standard (9-OHD,  $m/z$  350) and normalized according to their respective instrumental  
210 response factors, derived from solutions of known biomarker concentration, and  
211 sediment masses (Belt et al., 2012).

212 Concentrations of  $IP_{25}$  and HBI III were combined in the form of the  $P_{III}IP_{25}$  index  
213 (Eq. 4), with the latter then used to provide semi-quantitative estimates of spring sea ice  
214 concentration (SpSIC (%), Eq. 5) according to a recent regional calibration (Smik et al.,  
215 2016). A root mean-square error of 11% associated with SpSIC estimates, was also  
216 calculated using regional calibration data (Köseoğlu et al., 2018; Smik et al., 2016)

$$217 \quad P_{III}IP_{25} = \frac{IP_{25}}{(IP_{25} + (0.63 * HBI\ III))} \quad Eq\ (4)$$

$$218 \quad SpSIC\ (\%) = \frac{(P_{III}IP_{25} - 0.0692)}{0.0107} \quad Eq\ (5)$$

219 Finally, we used the non-parametric CP3O algorithm from the R package ECP (R Core  
220 Team, 2018) to carry out change-point analysis on SpSIC estimates to identify  
221 significant shifts in the time series profile (Supplementary Fig. S2). All biomarker and  
222 %SpSIC data are provided in Supplementary Data 2.

### 223 **2.3 Analysis of carbon**

224 Analyses of total carbon (TC) and organic carbon ( $C_{org}$ ) were performed with a LECO  
225 SC-632 at the Geological Survey of Norway, Trondheim. For TC determination,  
226 subsamples of 300-400 mg were combusted at 1350°C and the release of  $CO_2$  was  
227 measured. For  $C_{org}$  analysis, sub-samples of 400-450 mg were placed in carbon-free  
228 pervious ceramic combustion boats. These were placed on a heating plate at 50°C ( $\pm$   
229 5°C) and treated with 10 vol.% hydrochloric acid (HCl) to remove inorganic carbon

230 (carbonate) and subsequently rinsed with distilled water and dried in the drying oven  
231 prior to analysis. Carbonate content was calculated as  $\text{CaCO}_3 = (\text{TC} - \text{C}_{\text{org}}) \times 8.33$  with  
232 an assumption that calcite is the dominant form in the carbonate fraction (Vogt et al.,  
233 2001). Results are provided in weight percentage (wt. %) and the standard deviation of  
234 the TC and  $\text{C}_{\text{org}}$  measurements based on the repeated measurements of a standard  
235 was  $\pm 0.026$  wt% ( $1\sigma$ ,  $n=8$ ) and  $\pm 0.028$  wt. % ( $1\sigma$ ,  $n=11$ ), respectively.

#### 236 **2.4 Age control for sediments deposited at ODP Hole 910C**

237 The age constraints for 910C is based on correlation of bio-stratigraphic and  
238 magneto-stratigraphic datums with Hole 911A together with additional benthic stable  
239 isotope data from 910C for the Pliocene (2.44 – 5.76 Ma). The age model based on the  
240 tie points and associated uncertainties have already been discussed in previous studies  
241 (Grøsfjeld et al., 2014; Knies et al., 2014b; Mattingsdal et al., 2014). Briefly, five tie  
242 points formed the basis of the age model for our target interval between ~3.4 and 2.6  
243 Ma in 910C (see Supplementary Table S1). Two tie-points at 190 mbsf and 305 mbsf  
244 inferred from seismic correlation between 910C and 911A mark the magneto-  
245 stratigraphic boundaries at 2.58 Ma (Matuyama/Gauss) and 3.6 Ma (Gauss/Gilbert)  
246 (Mattingsdal et al., 2014). Support for this age model is provided by the biostratigraphic  
247 “Datum A” (~2.78 Ma) at ~223 mbsf in 910C (Sato and Kameo, 1996) and the glacial to  
248 interglacial oscillations of the benthic  $\delta^{18}\text{O}$  record of 910C (Knies et al., 2014a).  
249 Between “Datum A” (2.78 Ma) and the inferred Gauss/Gilbert boundary (3.6 Ma), we  
250 have originally applied an age model based on linear sedimentation rates between  
251 these two fix-points (Knies et al., 2014a). One major climate transition (i.e. MIS M2  
252 glaciation) expressed by a sharp increase in the global  $\delta^{18}\text{O}$  stack (Lisiecki and Raymo,

253 2005) (Supplementary Fig. S4) falls within our targeted time interval of 3.4 to 2.6 Ma.  
254 We used the more radiogenic  $\epsilon_{Nd}$  peak at 260.4 mbsf in 910C as an additional tie point  
255 to define the MIS M2 glaciation (Supplementary Table S1, Supplementary Fig. S5),  
256 corresponding to a pronounced IRD pulse in Hole 911A (Supplementary Fig. S6). The  
257 calculated sedimentation rates between fix points either side of this new tie point are  
258 within the same order of magnitude (8 to 15 cm/ka) thus justifying this additional age fix  
259 point. The age of the “Datum A” corresponding to the depth 223 mbsf was constrained  
260 based on the occurrence of calcareous nanofossils in 910C and 911A (Sato and  
261 Kameo, 1996) and is slightly shifted from the original age of 2.78 Ma (Knies et al.,  
262 2014b) to 2.83 Ma in the revised age model (Supplementary Table S1). Together with  
263 the new tie points for biostratigraphic “Datum A” and shifted radiogenic  $\epsilon_{Nd}$  peak to MIS  
264 M2, we used the linear sedimentation rates between all tie points to establish the age  
265 model for 910C between 3.4 - 2.6 Ma (Supplementary Table S1). Based on the revised  
266 chronology, the most negative excursion in the authigenic  $\epsilon_{Nd}$  profile is now shifted from  
267 2.981 to 3.081 Ma, while the most positive excursion defines the MIS M2 glaciation  
268 (Supplementary Fig. S4). Considering the uncertainty in our age model, it might be  
269 challenging to resolve all individual peaks and troughs corresponding to glacial-  
270 interglacial stages in our proxy records of authigenic  $\epsilon_{Nd}$ , biomarkers and  $CaCO_3$ ;  
271 however, the most prominent excursions in our proxy records during the mPWP can be  
272 resolved with confidence, which is the primary target interval of the present study. All  
273 information on previously published and new tie points are provided in Supplementary  
274 Table S1.

275

## 276 **3. Results**

### 277 **3.1 Authigenic $\epsilon_{Nd}$ record from the Yermak Plateau.**

278 The new  $\epsilon_{Nd}$  record from the Yermak Plateau allows identification of the maximum limit  
279 of water mass exchange between the NAC and Arctic derived PW, particularly during  
280 the major climatic transitions of the Pliocene to the earliest Pleistocene (3.4–2.6 Ma).  
281 These include the MIS M2 glaciation (3.312–3.264 Ma), the mPWP (3.264–3.025 Ma)  
282 and the intensification of Northern Hemispheric glaciation (iNHG) at ~2.7 Ma ago. The  
283 authigenic  $\epsilon_{Nd}$  record shows long-term secular changes from -9.2 during the MIS M2  
284 glacial period to -14.4 (5.2  $\epsilon_{Nd}$  unit) during the mPWP; the modern value of -11.7  
285 reported (Lambelet et al., 2016) from the core site falling within this range. Thereafter,  
286 an increasing trend up to -7.8 at ~2.6 Ma is clearly discernable, with several prominent  
287 positive excursions associated with iNHG cold stages (Fig. 2c). Our  $\epsilon_{Nd}$  record for  
288 910C exhibits a larger range (6.6  $\epsilon_{Nd}$  unit) compared to that of 911A (3.4  $\epsilon_{Nd}$  unit)  
289 (Teschner et al., 2016) within the time period 3.5 – 2.5 Ma (Fig. 2c), most likely due to  
290 the higher temporal resolution.

### 291 **3.2 Biomarker and $\text{CaCO}_3$ records.**

292 The occurrence of seasonal sea ice throughout the record is confirmed by the near  
293 continuous presence of the biomarkers  $\text{IP}_{25}$  and HBI III (Fig. 2d). Although the  
294 concentration of HBI III is mainly lower than that of  $\text{IP}_{25}$ , it is the more abundant  
295 biomarker during the mPWP (ca. 3.150–2.970 Ma), consistent with more productive  
296 open-water conditions, as also shown by the carbonate record, which reaches its  
297 highest values during the MIS KM1-K2 (~3.150-3.050 Ma) (Fig. 2f). The  $\text{CaCO}_3$   
298 abundance measured in the bulk sediments ranges from 0.5 to 6%; however, a sharp

299 three fold increase from the mean value ~2% to 6% is evident during the mPWP, which  
300 coincides with the prominent negative excursion in the  $\epsilon_{Nd}$  record (Fig. 2c).

301

## 302 **4. Discussion**

303 The authigenic ferromanganese oxyhydroxide fraction extracted from the bulk  
304 sediments has been demonstrated to record the  $\epsilon_{Nd}$  signal of bottom waters of the  
305 Yermak Plateau (Teschner et al., 2016; Werner et al., 2014). Hence, temporal variations  
306 in authigenic  $\epsilon_{Nd}$  during glacial-interglacial periods have been primarily attributed to  
307 watermass exchange between the NAC and PW, changes in sediment provenance, and  
308 variable weathering input due to glacial erosion (Teschner et al., 2016). However, other  
309 factors/mechanisms that contributed to the past authigenic  $\epsilon_{Nd}$  variability are discussed  
310 in the following section.

### 311 **4.1 Factors contributing to past authigenic $\epsilon_{Nd}$ variability**

312 ODP Hole 910C is placed in the mixing zone between Atlantic- and Arctic-  
313 derived waters (Fig. 1) and is therefore well suited to monitor the relative influence of  
314 two water masses: (i) relatively warmer, high salinity water (i.e. the NAC characterized  
315 by a less radiogenic Nd isotope signature and (ii) relatively cold and less saline water  
316 (i.e. Arctic-derived PW) characterized by more radiogenic Nd isotopes. In the open  
317 ocean away from ocean margins and regions of deep-water formation, Nd appears to  
318 behave quasi-conservatively (Rempfer et al., 2011). Therefore, the variability in  
319 authigenic  $\epsilon_{Nd}$  record from the open ocean is mainly explained by the mixing of water  
320 masses with distinct  $\epsilon_{Nd}$  signatures (Lang et al., 2016). However, contributions from  
321 other sources of dissolved Nd can substantially influence the authigenic  $\epsilon_{Nd}$  record.

322 Assuming that the modern geological and tectonic setting of the study region have  
323 largely remained stable over the past ~4.6 Ma (Knies et al., 2014a), we discuss the  
324 following potential mechanisms and factors that may have contributed to the variability  
325 and changes in the authigenic  $\epsilon_{Nd}$  record of 910C: (i) changes in weathering regimes  
326 and sediment sources; (ii) boundary exchange processes; and (iii) volumetric exchange  
327 of the NAC and PW.

328         Dissolved radiogenic isotope signatures in seawater originate from weathering  
329 processes of the continental crust (Frank, 2002) and, therefore, the glacial-interglacial  
330 changes in chemical weathering could influence the  $\epsilon_{Nd}$  record. Teschner et al. (2016)  
331 reconstructed past water mass mixing and erosional inputs prior and post intensification  
332 of Northern Hemisphere glaciation (iNHG, ~2.7 million years ago) based on records of  
333 radiogenic isotopes of Sr, Nd and Pb at ODP Hole 911A. Changes in the authigenic  $\epsilon_{Nd}$   
334 record were highlighted for two different scenarios; (i) prior to the iNHG, the Pb and Nd  
335 isotopes composition was characterized by unradiogenic values and low variability due  
336 to the limited extent of ice sheets. These observations are consistent with earlier  
337 inferences from the Arctic Ocean (Haley et al., 2007) and suggest constant erosional  
338 supply of material to the Yermak Plateau, most likely from local sources (i.e. Svalbard).  
339 (ii) After the iNHG, conditions changed dramatically with higher-amplitude  $\epsilon_{Nd}$  variability  
340 in both deep waters and detrital sediments inputs due to changes in weathering inputs  
341 associated with the waxing and waning of the Eurasian ice sheets, water mass  
342 exchange and increased supply of ice-rafted debris (IRD). Comparison of the IRD  
343 record (Knies et al., 2014b) with our  $\epsilon_{Nd}$  record, shows higher IRD flux during the  
344 periods of MIS M2 glaciation and iNHG (~2.7 Ma), and low and stable IRD fluxes during

345 the mPWP (Supplementary Fig. S6). The latter corresponds to the IRD record from  
346 Site U1307 on Eirik Drift where coarse IRD is largely absent during the mPWP, and IRD  
347 is only present in small abundances during (de)glacials between ~3 Ma and 2.75 Ma.  
348 Therefore, higher variability in IRD supply and change of its sources could influence the  
349 authigenic  $\epsilon_{Nd}$  record in 910C; however, this can be excluded for the interglacial periods  
350 prior to the iNHG, particularly during the mPWP. It is also important to note that the  
351 timing of the iNHGs was further shifted to post MIS G2 (2.64 Ma) based on the Pb  
352 isotope and geochemical studies of the IRD on the lower eastern flank of the Reykjanes  
353 Ridge (Bailey et al., 2013). Therefore, we suggest that the observed variability and  
354 changes in the radiogenic Nd isotope record in 910C is affected by glacial weathering  
355 input probably during the MIS M2 glaciation and after the iNHG. In contrast, it is unlikely  
356 to be significantly affected by the changes in chemical weathering inputs and/sediment  
357 transport from distant sources during our targeted time interval of mPWP due to the  
358 stability of the climatic conditions and glacial erosion was rather limited.

359 The chemical weathering of Iceland-derived basaltic material can influence the  
360 Nd isotope composition of the NAC resulting in a shift towards more radiogenic values.  
361 However, in an earlier study, it has been suggested that present day exchange with  
362 Iceland derived basaltic material does not affect the deep water  $\epsilon_{Nd}$  signature of the  
363 main path of North Atlantic inflow, although it can influence the signature of southward  
364 flowing currents such as the East Greenland Current (Chen et al., 2012; Lacan and  
365 Jeandel, 2004).

366 Seawater interactions with the continental margins (boundary exchange) could  
367 be a potential source for radiogenic isotope signatures of seawater, particularly in the



368 Nordic Seas where basaltic formations are highly susceptible to dissolution and  
369 exchange with seawater (Chen et al., 2012; Lacan and Jeandel, 2004). The effects of  
370 boundary exchange have been reported from different continental margins in the  
371 subpolar regions including the Nordic Seas, and model results confirmed the  
372 importance of this input mechanism (Rempfer et al., 2011). Due to the large shelf areas  
373 of the Arctic Ocean, boundary exchange might be expected to be significant, although  
374 the water column data available so far do not provide clear evidence for this process  
375 (Andersson et al., 2008). Further, Laupkert et al (2017) suggested recently that  $\epsilon_{Nd}$   
376 values around -10 are present in the eastern and western Fram Strait below ~500 m,  
377 implying that there is no evidence for boundary exchange processes influencing the  $\epsilon_{Nd}$   
378 record to a significant extent on the Yermak Plateau.

379 In summary, with the absence of any significant ice-rafting prior to ~2.7 Ma  
380 (except MIS M2) in the Nordic Seas (Fig. 2e), increased sea surface temperatures  
381 (SST) by 3–7°C (Lawrence et al., 2009) between 3.4 and 2.6 Ma compared to the  
382 Holocene mean annual SST (Fig. 2g; dashed line) (Calvo et al., 2002), and thus no  
383 widespread Northern Hemisphere glacial advances, we attribute the large range in  $\epsilon_{Nd}$  (-  
384 14.8 to -9.0) in 910C prior to the iNHG to changes in watermass circulation rather than  
385 to variable glacial weathering input. As such, the prominent negative excursion in the  
386  $\epsilon_{Nd}$  record during the mPWP (i.e. -14.4  $\epsilon_{Nd}$  units; Fig. 2c) is most likely due to an  
387 increase in volume transport of the NAC, resulting in an Atlantic-dominated climate  
388 regime of the Eurasian sector of the Arctic Ocean. Further, the prominent negative  
389 excursion in  $\epsilon_{Nd}$  record coincides with a sharp three-fold increase in  $CaCO_3$  abundance  
390 during the mPWP (Fig. 2f). This suggests an increased flow of warm NAC with higher

391 pH resulted in better preservation of carbonate and/or increase in productivity during  
392 interglacial periods in the eastern Fram Strait (Supplementary Figs. S7b, d, e),  
393 consistent with earlier reports from modern and Quaternary sediments (Huber et al.,  
394 2000).

395 To test the hypothesis of increased “Atlantification” and its concurrent sea ice  
396 decline further, we quantified the volumetric changes of the AW-derived water masses  
397 and sea ice concentration at 910C using (1) a simplified binary mixing model by  
398 constraining the end member values of  $\epsilon_{Nd}$  for two water masses and (2) semi-  
399 quantitative estimates of spring sea ice concentration (%SpSIC) based on a regional  
400 calibration of biomarker distributions in modern sediments (Smik et al., 2016).

#### 401 **4.2 Quantifying water mass exchange based on authigenic $\epsilon_{Nd}$ record**

402 Compilation and reassessment of seawater Nd data from the literature shows  
403 that the characteristic NAC  $\epsilon_{Nd}$  signature near its origin in the inter-gyre region (north of  
404 46° N) displays  $\epsilon_{Nd}$  values between  $-14.0 \pm 0.3$  and  $-15.1 \pm 0.3$  (Dubois-Dauphin et al.,  
405 2017), which changes gradually during transport across the Arctic Mediterranean due to  
406 mixing of more radiogenic signatures of PW ( $\epsilon_{Nd} = -9.9 \pm 0.7$ , 1 SD (standard deviation)  
407 and  $[Nd] = 27.1$ ) (Laukert et al., 2017). We have assigned  $\epsilon_{Nd}$  and  $[Nd]$  values for the  
408 NAC ( $-15 \pm 1$  (1 SD) and  $16 \pm 1$  pmol/kg) and PW ( $-9.9 \pm 1$  (1 SD) and  $27 \pm 1$  pmol/kg)  
409 end-members, respectively, which are clearly distinct from the modern value in the  
410 Fram Strait (mean  $\epsilon_{Nd} = -11.7 \pm 0.8$  (2SD)) (Laukert et al., 2017). With this identification  
411 of suitable end-member values for  $\epsilon_{Nd}$ , we therefore adopt a simple binary mixing  
412 approach for the determination of the percentage Atlantic water component (%AWC) on  
413 the assumption that Nd behaves quasi-conservatively and end-member compositions

414 were invariant during the studied time interval. Such assumptions are discussed in more  
 415 detail in the Supplementary Note 2. Meanwhile, we note that this method was  
 416 successfully employed in a previous study (Lang et al., 2016) using a Nd isotope record  
 417 from the late Pliocene (3.3–2.4 Ma ago) to quantify the mixing proportion of southern  
 418 source water and north Atlantic deep water (NADW) in the North Atlantic.

#### 419 **4.2.1 Binary estimates of Atlantic water mass mixing using authigenic $\epsilon_{Nd}$ record**

420 We have used the  $\epsilon_{Nd}$  record from 910C to generate the semi-quantitative estimate of  
 421 water-mass mixing between NAC and PW during the Late Pliocene to early Pleistocene  
 422 (~3.4 - 2.6 Ma). The underlying assumptions of this approach are: (i) Nd isotopes exhibit  
 423 quasi-conservative behaviour, (ii) mixing of Atlantic- and Arctic-derived waters at 910C  
 424 is binary, and (iii) modern day end-members have been invariant between 3.4 and 2.6  
 425 Ma. We used the following binary mixing equation constrained by our current  
 426 understanding of end-member compositions:

$$427 \quad \epsilon_{Nd_{910C}} = \frac{\epsilon_{Nd_{AW}} * C_{AW} * f_{AW} + \epsilon_{Nd_P} * C_{PW} * f_{PW}}{C_{AW} * f_{AW} + C_{PW} * f_{PW}} \quad Eq (2)$$

$$428 \quad f_{AW} + f_{PW} = 1 \quad Eq (3)$$

429 where  $\%AWC_{\epsilon_{Nd}} = f_{AW} * 100$  is the relative contribution of Atlantic water component to  
 430 910C ( $\%PWC_{\epsilon_{Nd}} = 100 - \%AWC_{\epsilon_{Nd}}$ ),  $C_{PW}$  and  $C_{AW}$  represent the concentration of Nd in  
 431 the Arctic (PW) and the Atlantic (AW),  $\epsilon_{Nd910C}$  is the value of Nd isotope compositions of  
 432 sediment leach from 910C, and  $\epsilon_{AW}$  and  $\epsilon_{PW}$  are the end-members of isotope  
 433 composition of Atlantic and Arctic water masses, respectively.  $f_{AW}$  and  $f_{PW}$  represent the  
 434 fractions of Nd coming from the Atlantic (AW) and Arctic (PW) waters.

435 In order to validate the use of this binary mixing model to 910C, we also  
436 calibrated our approach by comparison of semi-quantitative estimates of modern day  
437 volume transport with in situ observations. We thus estimated the modern day volume  
438 transport of NAC using a contemporary  $\epsilon_{Nd}$  value at the borehole site of 910C and  
439 compared that with a mooring-based observation (Beszczynska-Moeller et al., 2012).  
440 Our estimate of %NAC based on  $\epsilon_{Nd}$  ( $47 \pm 9\%$ ) (Supplementary Fig. S9) compares well  
441 with a value of  $45 \pm 5\%$  (Supplementary Fig. S9b) measured from an array of moorings  
442 in Fram Strait ( $78^\circ 50' N$ ) over the period 1997–2010 (Beszczynska-Moeller et al.,  
443 2012).

444 We have determined the uncertainty associated fractions of NAC volume  
445 estimates using a Monte-Carlo error propagation method with 10,000 iterations in  
446 MATLAB, which is represented as an error envelop (at 95% confidence) (Fig. 3a).  
447 However, we offer some caution that our %NAC estimates may be subject to changes  
448 in the future when more suitable archives allow generation of orbital resolution records  
449 of NAC and PW end-member behaviour. For now, the uncertainties reported here for  
450 our  $\epsilon_{Nd}$ -based estimates of %NAC may be underestimated due to limited knowledge of  
451 end-member  $\epsilon_{Nd}$  values for Atlantic and Arctic waters. On the other hand, our main  
452 conclusions over our targeted time interval (3.4 – 2.6 Ma) are not influenced by such  
453 uncertainties.

454 Our estimates of %AWC in 910C indicate three distinct peaks with values close  
455 to 100%, indicating the presence of a dominant Atlantic watermass in the water column  
456 during the three interglacial events (Haywood et al., 2013) (i.e. MIS KM3, K1, and G17)  
457 within or close to the mPWP; albeit within the limitation of the age constraints of 910C

458 (Fig. 3 a). For MIS KM5c, with near-modern orbital configuration, the %AWC ( $51 \pm 11\%$ )  
459 was similar to today ( $45 \pm 5\%$ ) (Beszczynska-Moeller et al., 2012; Zhang et al., 2013)  
460 but was close to  $\sim 0\%$  during the preceding MIS M2 glaciation (3.305–3.285 Ma) (Fig.  
461 3a), consistent with previous observations of a weaker NAC and concurrent cooling in  
462 the circum-Arctic (De Schepper et al., 2015). Importantly, although %AWC estimates for  
463 the glacial periods (i.e. MIS M2 and iNHGs) might potentially suffer higher uncertainty  
464 due to enhanced IRD flux and weathering inputs associated with higher glacial activity,  
465 such effects during the mPWP are likely insignificant, in practice, due to the relatively  
466 stable climate and lower IRD fluxes (Blake-Mizen et al., 2019; Knies et al., 2014a) (Fig.  
467 2e and Supplementary Fig. S6). Pertinent to our reconstructed reduced flux of %AWC  
468 during the MIS M2 glaciation, we note that a similar situation has been reported for  
469 MIS6 based on authigenic coupled isotope records of Nd and Hf from the central Arctic  
470 Ocean (Chen et al., 2012).

#### 471 **4.2 Sea ice reconstruction**

472 Extensive sea ice cover ( $>60\%$  SpSIC) prevailed from 3.36–3.18 Ma, including  
473 maximum extent during MIS M2 (Fig. 3b). Thereafter, %SpSIC reduced substantially.  
474 According to Smik et al. (2016), biomarker-based %SpSIC estimates above ca. 68%  
475 also imply the occurrence of some summer sea ice ( $>5\%$  summer sea ice  
476 concentration (SuSIC)) (Supplementary Fig. S3). Similarly, while the occurrence of  
477 some summer sea ice was a common feature up to ca. 3.18 Ma (Fig. 3b), coincident  
478 with consistently low %AWC (i.e. below the modern value of 45%; Fig. 3a), ice-free  
479 summers were likely a common feature at the Yermak Plateau thereafter, especially  
480 during the mPWP. Change-point analysis carried out on our %SpSIC estimates shows

481 a statistically significant decrease of ca. 30–35% starting at ca. 3.15 Ma before  
482 increasing again at ca. 2.97 Ma (Supplementary Fig. S2). Prior to this, extensive sea ice  
483 cover similar to the modern (spring) maximum prevailed, including maximum extent  
484 during MIS M2 when the %AWC was at a minimum (Fig. 3a, b). The reduction in SpSIC  
485 during the mPWP likely reflects a response to increased %AWC, analogous to  
486 observations made for eastern Fram Strait (Spielhagen et al., 2011) and the Barents  
487 Sea spanning recent decades/centuries (Cabedo-Sanz and Belt, 2016). Similar  
488 observations have been reported for the Early Holocene and the Last Interglacial  
489 (MIS5e/Eemian), implying that increased Atlantic Water inflow is one important factor  
490 controlling sea ice conditions in an area covering northern Svalbard/Yermak Plateau  
491 and the northern Barents Sea continental margin (Belt et al., 2015; Müller et al., 2012;  
492 Stein et al., 2017). According to our SpSIC estimates, maximum sea ice extent during  
493 the mPWP exhibited a closer resemblance to that of modern-day late summer (i.e.  
494 minimum) conditions (Fig. 3b). These new data support the boundary conditions used in  
495 the Pliocene Research, Interpretation and Synoptic Mapping (PRISM) project, which  
496 assumes a conservative sea ice extent, an ice-free Arctic Ocean in summer, and winter  
497 sea ice conditions approximately equivalent to modern summer ice extent (Dowsett et  
498 al., 2010).

#### 499 **4.3 Forcing factors modulating North Atlantic volume transport and its impact**

500 Our new reconstructions of watermass mixing and carbonate abundances follow  
501 the periodicities of eccentricity (~100 ka), obliquity (~40) and precessional cycles (~20  
502 ka) (Figs. 4a, b). Further, the %AWC and %SpSIC records show good alignment with  
503 the eccentricity (Fig. 4c) and summer insolation in the northern hemisphere (Fig. 5b),

504 implying orbitally-paced control over changes to oceanic heat flow into the Arctic Ocean.  
505 Cross wavelet analysis highlights the common highest power between these two time  
506 series in colour bands (Fig. 4c). The vector arrows indicate an in-phase relation  
507 (pointing rightward) during 3.2 – 2.9 Ma at the eccentricity band (64 – 128 ka), implying  
508 that orbitally-controlled, enhanced NAC contribution resulted in an increase in marine  
509 productivity and reduction in sea ice coverage during the mPWP (Supplementary Fig.  
510 S7c, d). In particular, during the three interglacials with high eccentricity (i.e. KM3, K1,  
511 and G17; Fig. 5a, d), increased seasonality combined with warmer summers (higher  
512 solar insolation) in the Northern Hemisphere (Fig. 5a, b) may have resulted in an  
513 increased oceanic heat transport with consequential decline in Arctic sea ice extent and  
514 polar amplification of this warming. Alternatively, an orbitally-forced reduction in Arctic  
515 sea ice coverage may have changed buoyancy and salinity in the Atlantic, and thus  
516 been responsible for increased northward ocean heat transport during mPWP  
517 interglacials leading to a strongly positive ice-albedo feedback. Our proxy data do not  
518 reveal any correspondence with variable atmospheric CO<sub>2</sub> estimates (Fig. 5c, d and e)  
519 implying only a minor influence of greenhouse gas-derived radiative forcing in  
520 modulating NAC heat transport and reduction in Arctic sea ice. Further, tectonic  
521 changes could have driven circulation changes as has been reported for the Bering  
522 Strait and Nordic Sea related to reconfiguration of oceanic gateways (De Schepper et  
523 al., 2015; Horikawa et al., 2015). However, the strong signal of orbital cycles in our  
524 proxy records clearly indicate that the orbital forcing played the dominant role over all  
525 other controlling factors.

526           Based on multi-proxy records, it has been inferred that the Atlantic Meridional  
527 Overturning Circulation (AMOC) was significantly stronger in the mPWP compared to  
528 today (Raymo et al., 1996; Frank et al., 2002; Dowsett et al., 2009), which could have  
529 contributed to enhanced northward heat transport during the mPWP interglacials  
530 (Dowsett et al., 2009; Lawrence et al., 2010; Naafs et al., 2012), consistent with our  
531 findings. However, the exact mechanism(s) responsible for changes in northward heat  
532 transport remain a topic of debate (Haywood et al., 2016; Haywood et al., 2013; Zhang  
533 et al., 2013), but could potentially be resolved through further ocean modelling studies  
534 that integrate the new proxy data presented herein.

535           Regardless of the ultimate driver(s), our estimates of %AWC show a clear  
536 dominance of a warm and well-mixed Atlantic-dominated climate regime in the Eurasian  
537 Arctic during MIS KM3, K1, and (within the given age uncertainties) G17, with lower  
538 than modern sea ice extent (including ice-free summers) and higher marine productivity,  
539 consistent with modeled and reconstructed amplification of Arctic surface temperatures  
540 (Ballantyne et al., 2013), and a rise in annual mean surface air temperatures between  
541 4°C to 5°C ( $\Delta t = \text{Plio-KM5c} - \text{pre-industrial}$ ) (Prescott et al., 2018). This implies that the  
542 increase in %AWC with concurrent reduction in %SpSIC during these mPWP  
543 interglacials resembles modern observations of an advanced “Atlantification” of the  
544 study region (Cabedo-Sanz and Belt, 2016; Naafs et al., 2010; Spielhagen et al., 2011).

545           The conclusion of increased “Atlantification” of the Arctic during the mPWP from  
546 our new proxy records from the Atlantic-Arctic gateway confirms previous studies from  
547 lower latitudes a (Naafs et al., 2010; Raymo et al., 1996). Since current generation  
548 models have not yet been validated against any proxy-based observations of



549 “Atlantification” in the Eurasian sector of the Arctic during the mPWP, our new Nd  
550 isotope, biomarker and CaCO<sub>3</sub> records thus provide important input for testing the  
551 robustness of future climate modelling for northern high latitude settings.

## 552 **5. Conclusions**

553 Our new Nd isotope record of past water mass exchange in the Atlantic-Arctic  
554 gateway relative to the modern-day setting suggests a near doubling of NAC volume  
555 transport during mPWP interglacials KM3, K1, and G17 with different orbital  
556 configurations and thus stronger seasonality than today. This resulted in a warm and  
557 well-mixed Atlantic-dominated climate regime (“Atlantification”) of the Eurasian sector of  
558 the Arctic Ocean, reduced spring sea ice concentration, and the possibility of ice-free  
559 conditions during summers. In contrast, the mPWP interglacial with near-modern orbits  
560 (MIS KM5c) does not show significant deviation from today’s NAC volume transport or  
561 sea ice extent. This study demonstrates a dominant role of orbital forcing in modulating  
562 northward ocean heat transport and Arctic sea ice coverage during the mPWP. It also  
563 highlights the importance of improving data-model comparison studies for the Arctic  
564 Ocean that integrate reconstructions of water mass flow and ocean circulation, as well  
565 as temperature and sea ice, for climate states of the past that may be analogous to the  
566 future.

### 567 **Data availability**

568 All the data are provided in the supplementary and also will be archived in PANGEA upon acceptance of  
569 the manuscript.

### 570 **Code availability**

571 The MATLAB codes for uncertainty estimates on the volumetric water fractions of Atlantic water are  
572 available from the corresponding author W. Rahaman on request.

### 573 **Acknowledgements**

574 We acknowledge Ministry of Earth Sciences, Govt. of India, NCPOR, and Research Council of  
575 Norway through its funding scheme for CAGE (223259) and PACT (248793). We thank Manish  
576 Tiwari for his support as a Co-PI in the PACT project. We thank C Torrence, GP Compo, A  
577 Grinsted, JC Moore, and S Jevrejeva for MATLAB codes. Authors thank Priya Lokhande for  
578 initial handling of the sample for Nd isotope chemistry and Rohit Srivastava for providing  
579 MATLAB codes for Monte-Carlo error propagation. We thank two anonymous reviewers who  
580 provided supportive and constructive feedback on the initial version of this manuscript. Finally,  
581 we thank Laura F Robinson for editorial handling of the manuscript. The NCPOR Contribution  
582 number is J- 47/2020-21.

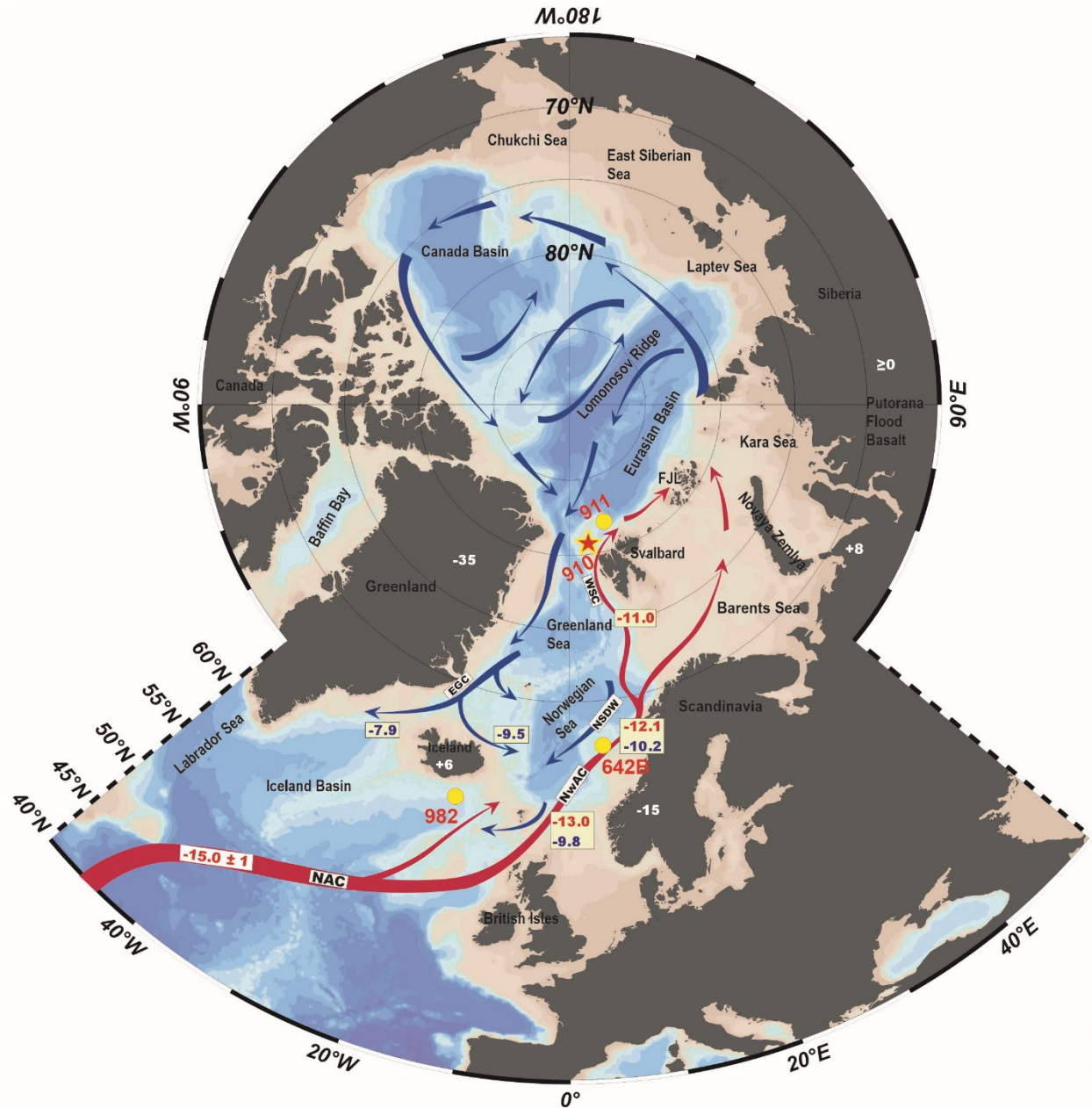
583

### 584 **Author contributions**

585 W.R., J.K. and M.T. designed the study. W.R., J.K., S.T.B and A.H wrote most of the text.  
586 Analysis of model results was completed by A.H and J.T. Mo.T. and L.N. analyzed authigenic  
587 Nd isotope compositions in bulk sediment. L.S, D.K and S.T.B. measured the concentrations of  
588 the  $IP_{25}$  and HBI III biomarkers in bulk sediments and interpreted outcomes. All authors  
589 contributed to interpreting results, discussion and improvement of this paper.

### 590 **Competing interests**

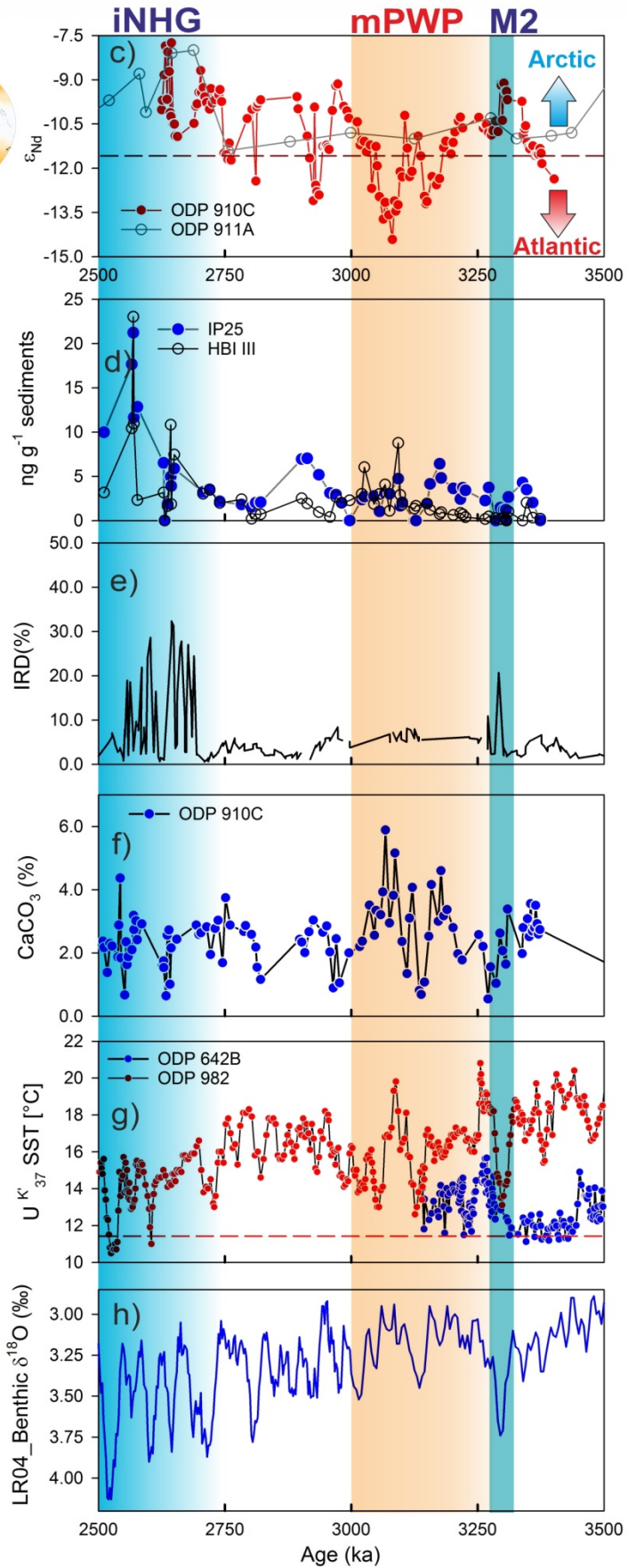
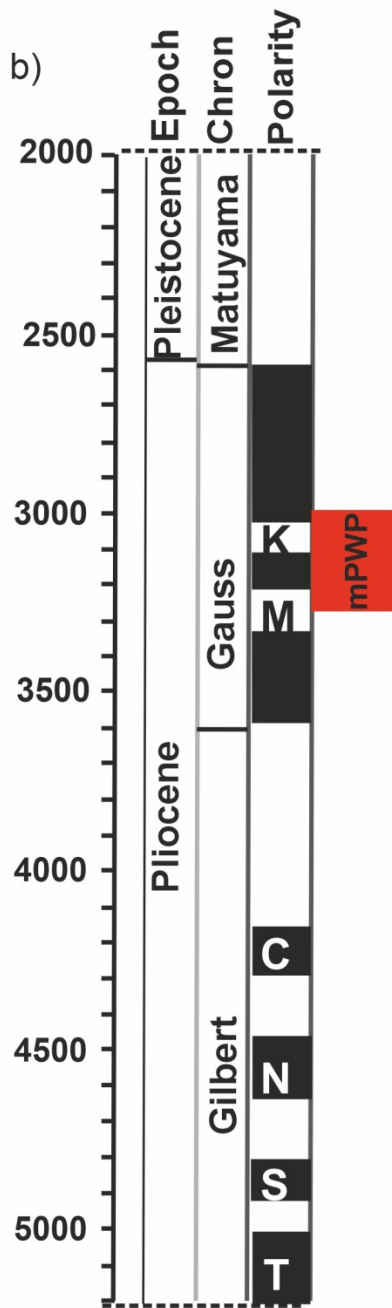
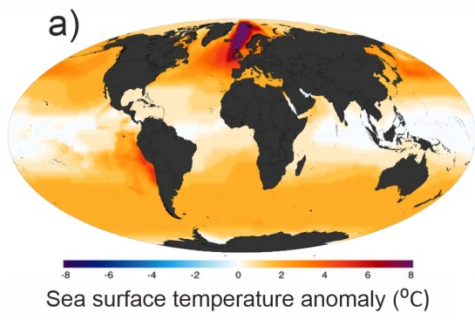
591 The authors declare no competing interests.



593

594 **Fig. 1. Water mass circulation and their characteristic Nd isotope compositions.** Locations of ODP  
 595 Sites 910 (red star) and 911 (filled yellow circle) with schematic flow paths of the main water masses in  
 596 the northern North Atlantic and Nordic Seas and their present-day  $\epsilon_{Nd}$  signatures (Teschner et al., 2016).  
 597 Dark red arrows mark the warm inflowing Atlantic water; dark blue arrows represent the cold deep and  
 598 surface water masses flowing out of the Arctic Ocean (Andersson et al., 2008; François and Catherine,

599 2004; Lacan and Jeandel, 2004). White numbers mark the average  $\epsilon_{\text{Nd}}$  values of the bedrocks of  
600 Svalbard(Tütken et al., 2002), the Norwegian Caledonian Margin and Iceland(Laskar et al., 2004), the  
601 Putorana basalts in Russia (Sharma et al., 1992), and Greenland (François and Catherine, 2004).  
602 Positions of ODP site 982 (58° N, 16° W) and ODP Hole 642B (67° 20' N, 2° 90' E) are shown.



604 **Fig. 2. Water mass exchange and associated changes in the Fram Strait during the Late-Pliocene**  
605 **and Pleistocene** (a) Sea surface temperature (SST) anomalies during the mPWP (~3.3 – 3.0 Ma)  
606 compared to today (Dowsett et al., 2009). b) Pliocene-Pleistocene time scale with paleo-magnetic  
607 reversals. Red block represents the time slice of mPWP. c) Authigenic  $\epsilon_{Nd}$  record from 910C (this study)  
608 and 911A (Teschner et al., 2016). d) Record of sea ice and open water biomarkers IP<sub>25</sub> and HBI III. (e)  
609 Record of IRD (%) from ODP site 911A (Knies et al., 2014b). f) Record of CaCO<sub>3</sub> abundance (wt. %). g)  
610 Record of alkenon UK<sub>37</sub> derived SST at ODP Sites 982 (Lawrence et al., 2009) (58° N, 16° W) and ODP  
611 Hole 642B (Bachem et al., 2017) (67° 20' N, 2° 90' E). Dashed lines indicate Holocene average SSTs for  
612 the Norwegian Sea (Calvo et al., 2002) at 11.6 °C. h) Benthic  $\delta^{18}O$  (LR04) stack (Lisiecki and Raymo,  
613 2005). The shaded bands represent the major climatic transitions: M2 glaciation (blue shade, 3.312–  
614 3.264 Ma), mid-Pliocene Warm Period (mPWP) (brown shade, 3.3–3.0 Ma) and intensification Northern  
615 Hemisphere glaciation (iNHG, ~2.7 Ma).

616

617

618

619

620

621

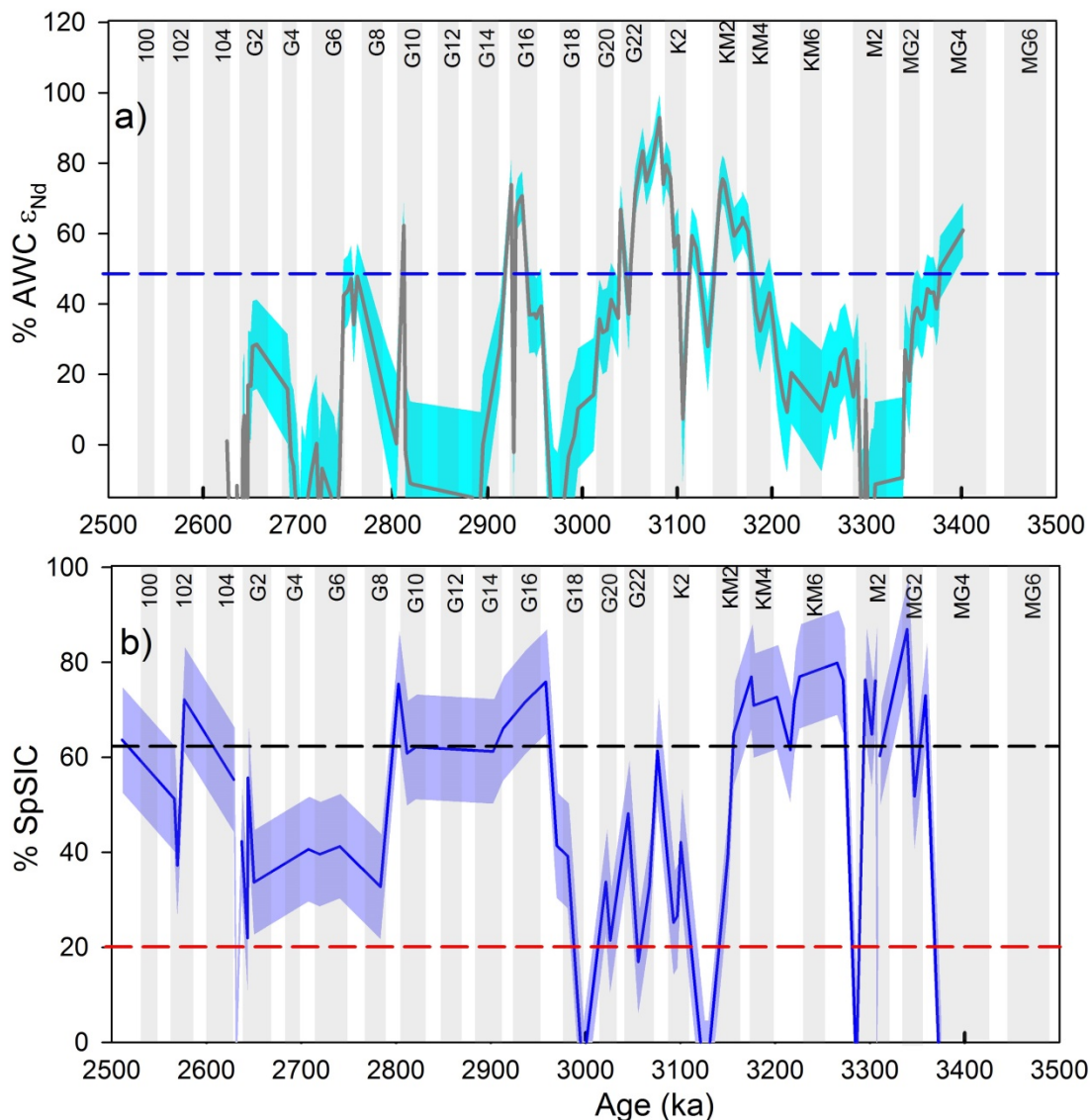
622

623

624

625

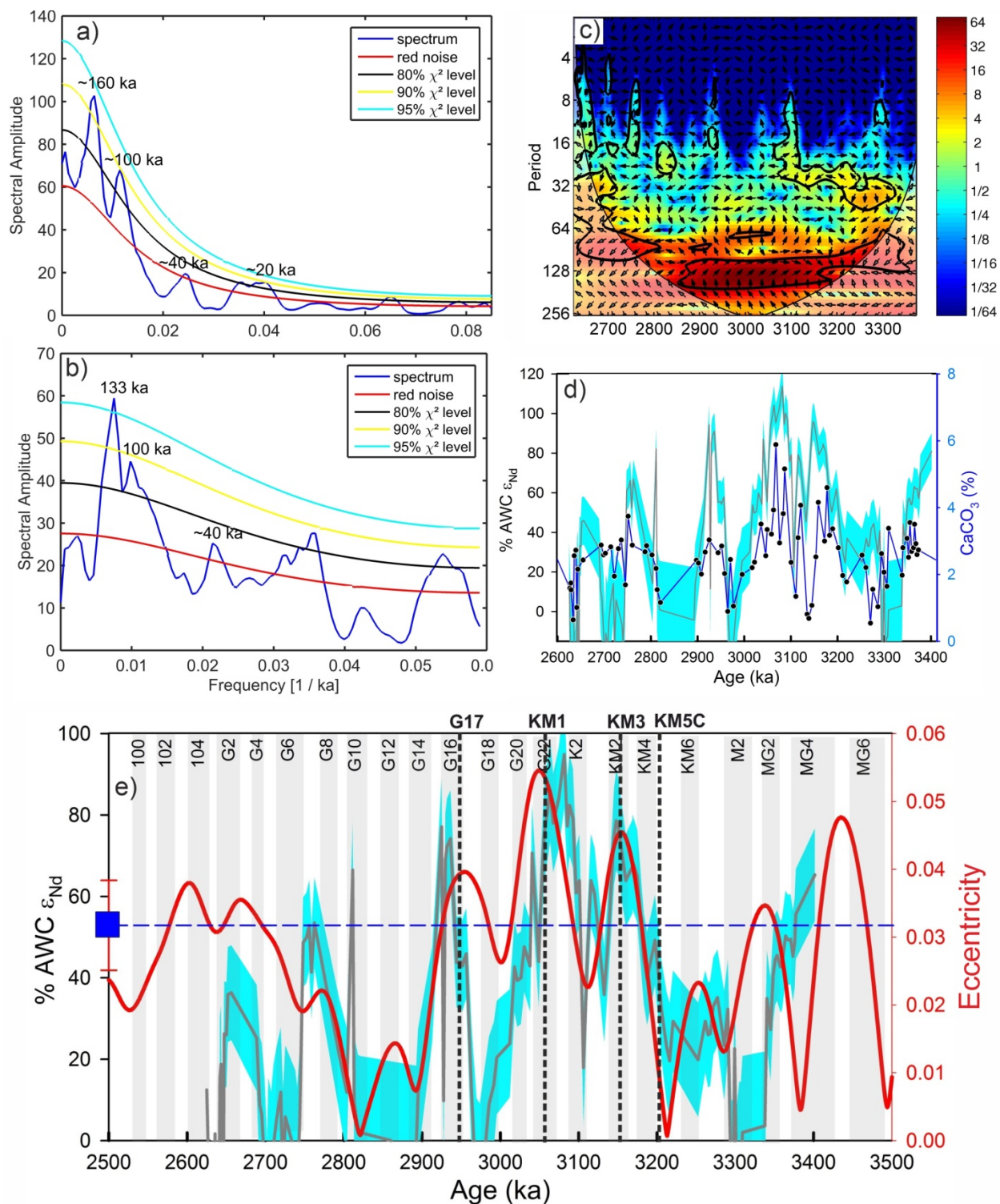
626



627

628 **Fig. 3. North Atlantic (NAC) volume transport and corresponding Arctic Sea Ice changes.** a)  
 629 Fraction of Atlantic Water Component (%AWC $\epsilon_{Nd}$ ). Dark gray line: Best estimate. Shading: 95%  
 630 confidence interval. Blue dashed line indicates modern Atlantic flow based on mooring estimate  
 631 (Beszczynska-Moeller et al., 2012). (b) Spring sea ice (%). Solid blue line represents mean value. Blue  
 632 shade represents root-mean-square error (RMSE) on the mean value. Blue and red dashed horizontal  
 633 lines represent the modern mean (1988-2017, NSIDC) sea ice maximum (62%, Apr-June; spring) and  
 634 minimum (20%, September; late summer) concentrations at the core site.



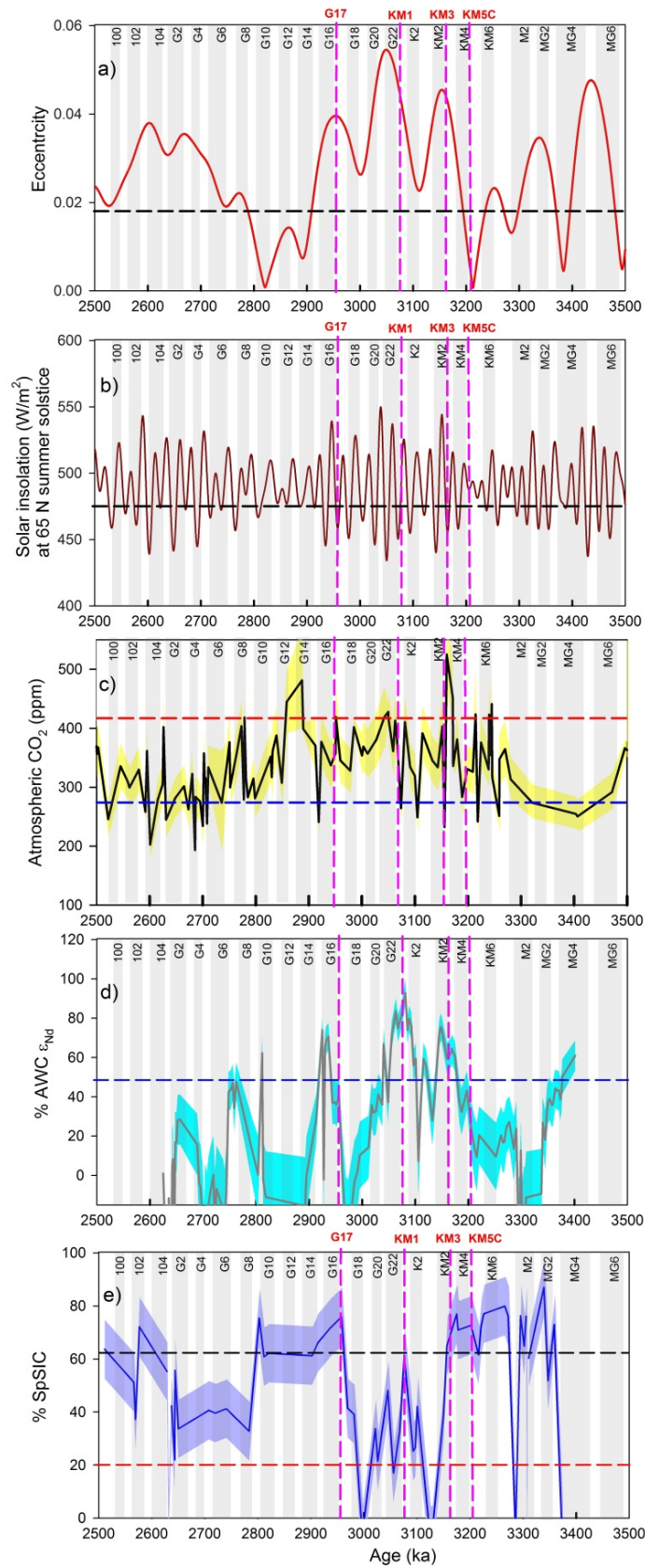


636

637 **Fig. 4. Identification of orbital cycles in proxy records.** Power spectrum analysis of (a) NAC volume  
 638 transport and (b) CaCO<sub>3</sub> abundance (%) records from the Yermak Plateau. They show periodicities of



639 orbital cycles at different significance level. c) Cross wavelet analysis of two time series highlights the  
640 common highest power between these two time series which is highlighted in color code. Vector arrow  
641 indicates phase relation between the time series. The 5% significance level against red noise is shown as  
642 a thick contour. The thin solid line indicates cone of influence. The relative phase relationship is shown as  
643 arrows (with in-phase pointing right, anti-phase pointing left, and  $\epsilon_{Nd}$  leading  $CaCO_3$  by  $90^\circ$  pointing  
644 straight down and vice versa). d) Comparison of the record of NAC with  $CaCO_3$  percentage, an indicator  
645 of marine productivity and preservation. Both the curves overall follow the same pattern; the highest  
646 abundance in calcium carbonate and thus the highest productivity was observed during mPWP when  
647 NAC flow was maximum. e) Reconstructed NAC (%) record is compared with the eccentricity record  
648 (Laskar et al., 2004). Vertical dashed lines represent super interglacials (Haywood and Valdes, 2004).  
649 Horizontal blue dashed line represents modern day NAC (%) in the Fram-Strait.



651 **Fig. 5. Role of orbital forcing in modulating watermass exchange and spring sea ice extent.** (a)  
652 Record of eccentricity (Laskar et al., 2004). Dashed horizontal line represents modern eccentricity.  
653 Vertical dashed lines (pink) indicate four interglacial periods KM5C, KM3, KM1 and G17. Among these  
654 four interglacial periods, KM5C is most similar to that of the modern orbital forcing (Haywood and Valdes,  
655 2004). (b) Record of solar insolation at 60° N summer solstice (Laskar et al., 2004). Dashed line  
656 represents modern value of summer insolation. c) Record of atmospheric pCO<sub>2</sub> derived from boron  
657 isotopes ( $\delta^{11}\text{B}$ ) (Foster et al., 2017). Yellow band represents error envelopes ( $1\sigma$  SD). Black and red colour  
658 dashed lines represent pre-industrial CO<sub>2</sub> (280 ppm) and present CO<sub>2</sub> (~410 ppm) level. These forcing  
659 parameters are compared with fraction of d) Atlantic Water (%AWC) and (e) Spring sea ice (%).

660

661

662

663

664

665

666

667

668

669

670

671

672 **References**

- 673 Andersson, P.S., Porcelli, D., Frank, M., Björk, G., Dahlqvist, R., Gustafsson, Ö., 2008.  
674 Neodymium isotopes in seawater from the Barents Sea and Fram Strait Arctic–  
675 Atlantic gateways. *Geochimica et Cosmochimica Acta* 72, 2854-2867.
- 676 Bachem, P.E., Risebrobakken, B., De Schepper, S., McClymont, E.L., 2017. Highly  
677 variable Pliocene sea surface conditions in the Norwegian Sea. *Clim. Past* 13,  
678 1153-1168.
- 679 Bailey, I., Hole, G.M., Foster, G.L., Wilson, P.A., Storey, C.D., Trueman, C.N., Raymo,  
680 M.E., 2013. An alternative suggestion for the Pliocene onset of major northern  
681 hemisphere glaciation based on the geochemical provenance of North Atlantic  
682 Ocean ice-rafted debris. *Quaternary Science Reviews* 75, 181-194.
- 683 Ballantyne, A.P., Axford, Y., Miller, G.H., Otto-Bliesner, B.L., Rosenbloom, N., White,  
684 J.W.C., 2013. The amplification of Arctic terrestrial surface temperatures by  
685 reduced sea-ice extent during the Pliocene. *Palaeogeography,*  
686 *Palaeoclimatology, Palaeoecology* 386, 59-67.
- 687 Belt, S.T., 2018. Source-specific biomarkers as proxies for Arctic and Antarctic sea ice.  
688 *Organic Geochemistry* 125, 277-298.
- 689 Belt, S.T., Brown, T.A., Rodriguez, A.N., Sanz, P.C., Tonkin, A., Ingle, R., 2012. A  
690 reproducible method for the extraction, identification and quantification of the  
691 Arctic sea ice proxy IP25 from marine sediments. *Analytical Methods* 4, 705-  
692 713.
- 693 Belt, S.T., Cabedo-Sanz, P., Smik, L., Navarro-Rodriguez, A., Berben, S.M.P., Knies, J.,  
694 Husum, K., 2015. Identification of paleo Arctic winter sea ice limits and the

695 marginal ice zone: Optimised biomarker-based reconstructions of late  
696 Quaternary Arctic sea ice. *Earth and Planetary Science Letters* 431, 127-139.

697 Berends, C.J., de Boer, B., Dolan, A.M., Hill, D.J., van de Wal, R.S.W., 2019. Modelling  
698 ice sheet evolution and atmospheric CO<sub>2</sub> during the Late Pliocene. *Clim. Past*  
699 15, 1603-1619.

700 Beszczynska-Moeller, A., Fahrbach, E., Schauer, U., Hansen, E., 2012. Variability in  
701 Atlantic water temperature and transport at the entrance to the Arctic Ocean,  
702 1997-2010.

703 Blake-Mizen, K., Hatfield, R.G., Stoner, J.S., Carlson, A.E., Xuan, C., Walczak, M.,  
704 Lawrence, K.T., Channell, J.E.T., Bailey, I., 2019. Southern Greenland glaciation  
705 and Western Boundary Undercurrent evolution recorded on Eirik Drift during the  
706 late Pliocene intensification of Northern Hemisphere glaciation. *Quaternary*  
707 *Science Reviews* 209, 40-51.

708 Cabedo-Sanz, P., Belt, S.T., 2016. Seasonal sea ice variability in eastern Fram Strait  
709 over the last 2000 years. *arktos* 2, 22.

710 Calvo, E., Grimalt, J., Jansen, E., 2002. High resolution U37K sea surface temperature  
711 reconstruction in the Norwegian Sea during the Holocene. *Quaternary Science*  
712 *Reviews* 21, 1385-1394.

713 Chen, T.-Y., Frank, M., Haley, B.A., Gutjahr, M., Spielhagen, R.F., 2012. Variations of  
714 North Atlantic inflow to the central Arctic Ocean over the last 14 million years  
715 inferred from hafnium and neodymium isotopes. *Earth and Planetary Science*  
716 *Letters* 353-354, 82-92.

717 Chow, N., Morad, S., Al-Aasm, I., 1996. Origin of Authigenic Carbonates in Eocene to  
718 Quaternary Sediments from the Arctic Ocean and Norwegian-Greenland Sea.  
719 Proceedings of the Ocean Drilling Program, Scientific Results 151.

720 Clotten, C., Stein, R., Fahl, K., De Schepper, S., 2018. Seasonal sea ice cover during  
721 the warm Pliocene: Evidence from the Iceland Sea (ODP Site 907). Earth and  
722 Planetary Science Letters 481, 61-72.

723 De Schepper, S., Schreck, M., Beck, K.M., Matthiessen, J., Fahl, K., Mangerud, G.,  
724 2015. Early Pliocene onset of modern Nordic Seas circulation related to ocean  
725 gateway changes. Nature Communications 6, 8659.

726 Ding, Q., Schweiger, A., L'Heureux, M., Steig, E.J., Battisti, D.S., Johnson, N.C.,  
727 Blanchard-Wrigglesworth, E., Po-Chedley, S., Zhang, Q., Harnos, K., Bushuk,  
728 M., Markle, B., Baxter, I., 2018. Fingerprints of internal drivers of Arctic sea ice  
729 loss in observations and model simulations. Nature Geoscience.

730 Dowsett, H., Robinson, M., Haywood, A.M., Salzmann, U., Hill, D., Sohl, L.E., Chandler,  
731 M., Williams, M., Foley, K., Stoll, D.K., 2010. The PRISM3D paleoenvironmental  
732 reconstruction. Stratigraphy 7, 123-139.

733 Dowsett, H.J., Cronin, T.M., Poore, R.Z., Thompson, R.S., Whatley, R.C., Wood, A.M.,  
734 1992. Micropaleontological Evidence for Increased Meridional Heat Transport in  
735 the North Atlantic Ocean During the Pliocene. Science 258, 1133-1135.

736 Dowsett, H.J., Robinson, M.M., Foley, K.M., 2009. Pliocene three-dimensional global  
737 ocean temperature reconstruction. Clim. Past 5, 769-783.

738 Dowsett, H.J., Robinson, M.M., Haywood, A.M., Hill, D.J., Dolan, A.M., Stoll, D.K.,  
739 Chan, W.-L., Abe-Ouchi, A., Chandler, M.A., Rosenbloom, N.A., Otto-Bliesner,

740 B.L., Bragg, F.J., Lunt, D.J., Foley, K.M., Riesselman, C.R., 2012. Assessing  
741 confidence in Pliocene sea surface temperatures to evaluate predictive models.  
742 Nature Climate Change 2, 365.

743 Dubois-Dauphin, Q., Colin, C., Bonneau, L., Montagna, P., Wu, Q., Van Rooij, D.,  
744 Reverdin, G., Douville, E., Thil, F., Waldner, A., Frank, N., 2017. Fingerprinting  
745 Northeast Atlantic water masses using neodymium isotopes. *Geochimica et*  
746 *Cosmochimica Acta* 210, 267-288.

747 Foster, G.L., Royer, D.L., Lunt, D.J., 2017. Future climate forcing potentially without  
748 precedent in the last 420 million years. *Nature Communications* 8, 14845.

749 François, L., Catherine, J., 2004. Neodymium isotopic composition and rare earth  
750 element concentrations in the deep and intermediate Nordic Seas: Constraints  
751 on the Iceland Scotland Overflow Water signature. *Geochemistry, Geophysics,*  
752 *Geosystems* 5.

753 Frank, M., 2002. RADIOGENIC ISOTOPES: TRACERS OF PAST OCEAN  
754 CIRCULATION AND EROSIONAL INPUT. *Reviews of Geophysics* 40, 1-1-1-38.

755 Grøsfjeld, K., De Schepper, S., Fabian, K., Husum, K., Baranwal, S., Andreassen, K.,  
756 Knies, J., 2014. Dating and palaeoenvironmental reconstruction of the  
757 sediments around the Miocene/Pliocene boundary in Yermak Plateau ODP Hole  
758 911A using marine palynology. *Palaeogeography, Palaeoclimatology,*  
759 *Palaeoecology* 414, 382-402.

760 Haley, B.A., Frank, M., Spielhagen, R.F., Eisenhauer, A., 2007. Influence of brine  
761 formation on Arctic Ocean circulation over the past 15 million years. *Nature*  
762 *Geoscience* 1, 68.

763 Haywood, A.M., Dowsett, H.J., Dolan, A.M., 2016. Integrating geological archives and  
764 climate models for the mid-Pliocene warm period. *Nature Communications* 7,  
765 10646.

766 Haywood, A.M., Hill, D.J., Dolan, A.M., Otto-Bliesner, B.L., Bragg, F., Chan, W.L.,  
767 Chandler, M.A., Contoux, C., Dowsett, H.J., Jost, A., Kamae, Y., Lohmann, G.,  
768 Lunt, D.J., Abe-Ouchi, A., Pickering, S.J., Ramstein, G., Rosenbloom, N.A.,  
769 Salzmann, U., Sohl, L., Stepanek, C., Ueda, H., Yan, Q., Zhang, Z., 2013.  
770 Large-scale features of Pliocene climate: results from the Pliocene Model  
771 Intercomparison Project. *Clim. Past* 9, 191-209.

772 Haywood, A.M., Valdes, P.J., 2004. Modelling Pliocene warmth: contribution of  
773 atmosphere, oceans and cryosphere. *Earth and Planetary Science Letters* 218,  
774 363-377.

775 Horikawa, K., Martin, E.E., Basak, C., Onodera, J., Seki, O., Sakamoto, T., Ikehara, M.,  
776 Sakai, S., Kawamura, K., 2015. Pliocene cooling enhanced by flow of low-  
777 salinity Bering Sea water to the Arctic Ocean. *Nature Communications* 6, 7587.

778 Huber, R., Meggers, H., Baumann, K.H., Henrich, R., 2000. Recent and Pleistocene  
779 carbonate dissolution in sediments of the Norwegian–Greenland Sea. *Marine*  
780 *Geology* 165, 123-136.

781 IPCC, 2013. *Climate Change 2013: The Physical Science Basis*. Contribution of  
782 Working Group I to the Fifth Assessment Report of the Intergovernmental Panel  
783 on Climate Change. Cambridge University Press, Cambridge, United Kingdom  
784 and New York, NY, USA.



785 Kinnard, C., Zdanowicz, C.M., Fisher, D.A., Isaksson, E., de Vernal, A., Thompson,  
786 L.G., 2011. Reconstructed changes in Arctic sea ice over the past 1,450 years.  
787 Nature 479, 509.

788 Knies, J., Cabedo-Sanz, P., Belt, S.T., Baranwal, S., Fietz, S., Rosell-Melé, A., 2014a.  
789 The emergence of modern sea ice cover in the Arctic Ocean. Nature  
790 Communications 5, 5608.

791 Knies, J., Matthiessen, J., Vogt, C., Stein, R., 2002. Evidence of 'Mid-Pliocene (~3 Ma)  
792 global warmth' in the eastern Arctic Ocean and implications for the  
793 Svalbard/Barents Sea ice sheet during the late Pliocene and early Pleistocene  
794 (~3 – 1.7 Ma). Boreas 31, 82-93.

795 Knies, J., Mattingdal, R., Fabian, K., Grøsfjeld, K., Baranwal, S., Husum, K., De  
796 Schepper, S., Vogt, C., Andersen, N., Matthiessen, J., Andreassen, K., Jokat,  
797 W., Nam, S.-I., Gaina, C., 2014b. Effect of early Pliocene uplift on late Pliocene  
798 cooling in the Arctic–Atlantic gateway. Earth and Planetary Science Letters 387,  
799 132-144.

800 Köseoğlu, D., Belt, S.T., Husum, K., Knies, J., 2018. An assessment of biomarker-  
801 based multivariate classification methods versus the PIP25 index for paleo Arctic  
802 sea ice reconstruction. Organic Geochemistry 125, 82-94.

803 Lacan, F., Jeandel, C., 2004. Denmark Strait water circulation traced by heterogeneity  
804 in neodymium isotopic compositions. Deep Sea Research Part I: Oceanographic  
805 Research Papers 51, 71-82.

806 Lambelet, M., van de Flierdt, T., Crocket, K., Rehkämper, M., Kreissig, K., Coles, B.,  
807 Rijkenberg, M.J.A., Gerringa, L.J.A., de Baar, H.J.W., Steinfeldt, R., 2016.

808 Neodymium isotopic composition and concentration in the western North Atlantic  
809 Ocean: Results from the GEOTRACES GA02 section. *Geochimica et*  
810 *Cosmochimica Acta* 177, 1-29.

811 Lang, D.C., Bailey, I., Wilson, P.A., Chalk, T.B., Foster, G.L., Gutjahr, M., 2016.  
812 Incursions of southern-sourced water into the deep North Atlantic during late  
813 Pliocene glacial intensification. *Nature Geoscience* 9, 375.

814 Laskar, J., Robutel, P., Joutel, F., Gastineau, M., Correia, A.C.M., Levrard, B., 2004. A  
815 long-term numerical solution for the insolation quantities of the Earth. *A&A* 428,  
816 261-285.

817 Laukert, G., Frank, M., Bauch, D., Hathorne, E.C., Rabe, B., von Appen, W.-J., Wegner,  
818 C., Zieringer, M., Kassens, H., 2017. Ocean circulation and freshwater pathways  
819 in the Arctic Mediterranean based on a combined Nd isotope, REE and oxygen  
820 isotope section across Fram Strait. *Geochimica et Cosmochimica Acta* 202, 285-  
821 309.

822 Lawrence, K., Herbert, T., M. Brown, C., Raymo, M., M. Haywood, A., 2009. High  
823 amplitude variations in North Atlantic sea surface temperature during the Early  
824 Pliocene Warm Period.

825 Lisiecki, L.E., Raymo, M.E., 2005. A Pliocene-Pleistocene stack of 57 globally  
826 distributed benthic  $\delta^{18}\text{O}$  records. *Paleoceanography* 20.

827 Martin, F., 2002. RADIOGENIC ISOTOPES: TRACERS OF PAST OCEAN  
828 CIRCULATION AND EROSIONAL INPUT. *Reviews of Geophysics* 40, 1-1-1-38.

829 Mattingsdal, R., Knies, J., Andreassen, K., Fabian, K., Husum, K., Grøsfjeld, K., De  
830 Schepper, S., 2014. A new 6 Myr stratigraphic framework for the Atlantic–Arctic  
831 Gateway. *Quaternary Science Reviews* 92, 170-178.

832 Müller, J., Wagner, A., Fahl, K., Stein, R., Prange, M., Lohmann, G., 2011. Towards  
833 quantitative sea ice reconstructions in the northern North Atlantic: A combined  
834 biomarker and numerical modelling approach. *Earth and Planetary Science  
835 Letters* 306, 137-148.

836 Müller, J., Werner, K., Stein, R., Fahl, K., Moros, M., Jansen, E., 2012. Holocene  
837 cooling culminates in sea ice oscillations in Fram Strait. *Quaternary Science  
838 Reviews* 47, 1-14.

839 Naafs, B.D.A., Stein, R., Hefter, J., Khélifi, N., De Schepper, S., Haug, G.H., 2010. Late  
840 Pliocene changes in the North Atlantic Current. *Earth and Planetary Science  
841 Letters* 298, 434-442.

842 Petrie, R.E., Shaffrey, L.C., Sutton, R.T., 2015. Atmospheric Impact of Arctic Sea Ice  
843 Loss in a Coupled Ocean–Atmosphere Simulation. *Journal of Climate* 28, 9606-  
844 9622.

845 Polyakov, I.V., Pnyushkov, A.V., Alkire, M.B., Ashik, I.M., Baumann, T.M., Carmack,  
846 E.C., Goszczko, I., Guthrie, J., Ivanov, V.V., Kanzow, T., Krishfield, R., Kwok,  
847 R., Sundfjord, A., Morison, J., Rember, R., Yulin, A., 2017. Greater role for  
848 Atlantic inflows on sea-ice loss in the Eurasian Basin of the Arctic Ocean.  
849 *Science* 356, 285-291.

850 Prescott, C.L., Dolan, A.M., Haywood, A.M., Hunter, S.J., Tindall, J.C., 2018. Regional  
851 climate and vegetation response to orbital forcing within the mid-Pliocene Warm  
852 Period: A study using HadCM3. *Global and Planetary Change* 161, 231-243.

853 R Core Team, 2018. R: A language and environment for statistical computing. R  
854 Foundation for Statistical Computing. Vienna, Austria URL [http://www.R-](http://www.R-project.org/)  
855 [project.org/](http://www.R-project.org/).

856 Raymo, M.E., Grant, B., Horowitz, M., Rau, G.H., 1996. Mid-Pliocene warmth: stronger  
857 greenhouse and stronger conveyor. *Marine Micropaleontology* 27, 313-326.

858 Rempfer, J., Stocker, T.F., Joos, F., Dutay, J.-C., Siddall, M., 2011. Modelling Nd-  
859 isotopes with a coarse resolution ocean circulation model: Sensitivities to model  
860 parameters and source/sink distributions. *Geochimica et Cosmochimica Acta* 75,  
861 5927-5950.

862 Sato, T., Kameo, K., 1996. Pliocene to Quaternary calcareous nannofossil biostratig-  
863 raphy of the Arctic Ocean, with reference to late Pliocene glaciation. W.F. (Eds.),  
864 Proc. ODP, Sci. Results 151.

865 Sharma, M., Basu, A.R., Nesterenko, G.V., 1992. Temporal Sr-, Nd- and Pb-isotopic  
866 variations in the Siberian flood basalts: Implications for the plume-source  
867 characteristics. *Earth and Planetary Science Letters* 113, 365-381.

868 Smik, L., Cabedo-Sanz, P., Belt, S.T., 2016. Semi-quantitative estimates of paleo Arctic  
869 sea ice concentration based on source-specific highly branched isoprenoid  
870 alkenes: A further development of the PIP25 index. *Organic Geochemistry* 92,  
871 63-69.

872 Spielhagen, R.F., Werner, K., Sørensen, S.A., Zamelczyk, K., Kandiano, E., Budeus,  
873 G., Husum, K., Marchitto, T.M., Hald, M., 2011. Enhanced Modern Heat Transfer  
874 to the Arctic by Warm Atlantic Water. *Science* 331, 450-453.

875 Stein, R., Fahl, K., Gierz, P., Niessen, F., Lohmann, G., 2017. Arctic Ocean sea ice  
876 cover during the penultimate glacial and the last interglacial. *Nature*  
877 *Communications* 8, 373.

878 Tachikawa, K., Jeandel, C., Roy-Barman, M., 1999. A new approach to the Nd  
879 residence time in the ocean: the role of atmospheric inputs. *Earth and Planetary*  
880 *Science Letters* 170, 433-446.

881 Tanaka, T., Togashi, S., Kamioka, H., Amakawa, H., Kagami, H., Hamamoto, T.,  
882 Yuhara, M., Orihashi, Y., Yoneda, S., Shimizu, H., Kunimaru, T., Takahashi, K.,  
883 Yanagi, T., Nakano, T., Fujimaki, H., Shinjo, R., Asahara, Y., Tanimizu, M.,  
884 Dragusanu, C., 2000. JNdi-1: A neodymium isotopic reference in consistency  
885 with LaJolla neodymium.

886 Teschner, C., Frank, M., Haley, B.A., Knies, J., 2016. Plio-Pleistocene evolution of  
887 water mass exchange and erosional input at the Atlantic-Arctic gateway.  
888 *Paleoceanography* 31, 582-599.

889 Tütken, T., Eisenhauer, A., Wiegand, B., Hansen, B.T., 2002. Glacial–interglacial cycles  
890 in Sr and Nd isotopic composition of Arctic marine sediments triggered by the  
891 Svalbard/Barents Sea ice sheet. *Marine Geology* 182, 351-372.

892 Vogt, C., Knies, J., Spielhagen, R.F., Stein, R., 2001. Detailed mineralogical evidence  
893 for two nearly identical glacial/deglacial cycles and Atlantic water advection to

894 the Arctic Ocean during the last 90,000 years. *Global and Planetary Change* 31,  
895 23-44.

896 Werner, K., Frank, M., Teschner, C., Müller, J., F. Spielhagen, R., 2014. Neoglacial  
897 change in deep water exchange and increase of sea-ice transport through  
898 eastern Fram Strait: Evidence from radiogenic isotopes.

899 Zamelczyk, K., Rasmussen, T.L., Husum, K., Godtliobsen, F., Hald, M., 2014. Surface  
900 water conditions and calcium carbonate preservation in the Fram Strait during  
901 marine isotope stage 2, 28.8–15.4 kyr. *Paleoceanography* 29, 1-12.

902 Zhang, Z.S., Nisancioglu, K.H., Chandler, M.A., Haywood, A.M., Otto-Bliesner, B.L.,  
903 Ramstein, G., Stepanek, C., Abe-Ouchi, A., Chan, W.L., Bragg, F.J., Contoux,  
904 C., Dolan, A.M., Hill, D.J., Jost, A., Kamae, Y., Lohmann, G., Lunt, D.J.,  
905 Rosenbloom, N.A., Sohl, L.E., Ueda, H., 2013. Mid-pliocene Atlantic Meridional  
906 Overturning Circulation not unlike modern. *Clim. Past* 9, 1495-1504.

907

908

## SUPPLEMENTARY INFORMATION

### **Reduced Arctic sea ice extent during the mid-Pliocene Warm Period concurrent with increased Atlantic-climate regime**

\*Waliur Rahaman<sup>1</sup>, Lukas Smik<sup>2</sup>, Deniz Köseoğlu<sup>3</sup>, Lathika N<sup>1</sup>, Mohd Tarique<sup>1,4</sup>, Meloth Thamban<sup>1</sup>, Alan Haywood<sup>5</sup>, Simon T. Belt<sup>2</sup>, J. Knies<sup>3,6</sup>

<sup>1</sup> National Centre for Polar and Ocean Research (NCPOR), Ministry of Earth Sciences, Vasco-da-Gama, Goa 403804, India

<sup>2</sup> School of Geography, Earth and Environmental Sciences, University of Plymouth, PL4 8AA, UK

<sup>3</sup> CAGE – Centre for Arctic Gas Hydrate, Environment and Climate, Department of Geosciences, UiT The Arctic University of Norway, 9037 Tromsø, Norway

<sup>4</sup> Department of Marine Geology, Mangalore University, Mangalore, India

<sup>5</sup> School of Earth and Environment, University of Leeds, Woodhouse Lane, Leeds, LS2 9JT, UK

<sup>6</sup> Geological Survey of Norway, N-7491 Trondheim, Norway

## **This supplement contains the following**

S1. Modern physico-chemical conditions in the Fram Strait

S2. Constraining endmember compositions of NAC and PW

S3. Time series analysis to identify frequencies and their evolution

Table S1. Chronology of the ODP Hole 910C

Supplementary Data 1. Nd isotope data [separate Excel file\_ Data 1]

Supplementary Data 2. Biomarker and Spring Sea ice concentration [separate Excel file\_ Data 2]

Figure S1. Replicate analysis of Nd isotopes in authigenic phases.

Figure S2. Reconstruction of spring sea ice (SpSIC) record.

Figure S3. Summer and Spring Sea ice records.

Figure S4. Assessment of the chronology.

Figure S5. Chronology of the ODP 910C core.

Figure S6. Assessing the role of IRD supply on authigenic  $\epsilon_{Nd}$  variability

Figure S7. Physico-chemical distributions in the Fram-Strait water column.

Figure S8. Water mass distribution and their characteristic  $\epsilon_{Nd}$  signature.

Figure S9. Validation of water fraction estimates derived from Nd isotope mass balance



## **S1. Modern physico-chemical conditions in the Fram Strait**

In order to understand physico-chemical conditions in the mixing zone between two water masses i.e. North Atlantic current (NAC) and Arctic derived water mass (PW), we have plotted water column distribution of the physico-chemical parameters i.e. temperature-salinity and alkalinity-pH along a north-south transect (supplementary Fig. S6). This shows that the main flow of water into the Nordic Seas takes place over the Iceland-Faroe Ridge and Faroe-Shetland Channel, with a combined northward inflow of 7 SV (1 Sverdrup =  $10^6$  m<sup>3</sup>/s) (Blindheim and Østerhus, 2005). The subsurface Atlantic-derived water masses enter the Arctic Ocean as West Spitsbergen Current with mean temperatures of  $3.1 \pm 0.1^\circ\text{C}$  (Beszczynska-Moeller et al., 2012) (supplementary Fig. S6b). Further, alkalinity-pH distribution along the transect shows strong gradient (supplementary Fig. S6 d, e). The warm and high salinity NAC is characterized by higher alkalinity ( $>2400$   $\mu\text{mol/kg}$ ) and pH ( $>8$ ) whereas the cold and fresh Arctic derived waters are characterized by relatively lower alkalinity and pH.

## **S2. Constraining endmember compositions of NAC and PW**

The North Atlantic Current (NAC) is the northeastward extension of the modified Gulf Stream (supplementary Fig. S7) and is characterized by  $\epsilon_{\text{Nd}}$  values of -13.2 to -13.0 with an average [Nd] of  $16 \pm 1$  pmol/kg near Iceland-Faroe Ridge in the Nordic Sea ( $T>5^\circ\text{C}$ ;  $S>35.0$ ) (François and Catherine, 2004; Lacan and Jeandel, 2004a; Lacan and Jeandel, 2004b). The NAC surface water near its origin (above  $46^\circ$  N) displays  $\epsilon_{\text{Nd}}$  values between  $14.0 \pm 0.3$  and  $15.1 \pm 0.3$ , dominated by the subpolar gyre signature (supplementary Fig. S7c) (Dubois-Dauphin et al., 2017). Recent study of Nd composition in the vertical profiles samples along GEOTRACES transect GA02

(Lambelet et al., 2016) shows  $\epsilon_{Nd}$  near the origin of NAC ranging from -13 in the Irminger Sea to -17.0 in the South-East Labrador Sea (supplementary Fig. S7b). Considering glacial-interglacial variability in  $\epsilon_{Nd}$  values of NAC near its origin due the changes in the contribution of Labrador current and Gulf-stream, the endmember value of NAC could be shifted accordingly, however, they will be accommodated within the range of their uncertainty 1  $\epsilon_{Nd}$  unit ( $1\sigma$ ) with an average value of -15. Hence, we have assigned the endmember values of NAC  $-15 \pm 1$   $\epsilon_{Nd}$  unit ( $1\sigma$ ) and  $16 \pm 1$  pmol/kg for [Nd]. For Arctic-derived polar waters (PW), Laukert et al. (2017) report  $\epsilon_{Nd}$  and [Nd] values in the Fram Strait  $-9.9 \pm 1$ , 1 SD and 27.1 pmol/kg respectively (Laukert et al., 2017). These endmember values and their uncertainty in binary mixing model can explain the total variability reflected in our  $\epsilon_{Nd}$  record except few radiogenic peaks associated with the cold stages. The AW entering the Arctic Ocean through the Fram Strait is characterized by  $\epsilon_{Nd} \approx -11.7$  and [Nd]  $\approx 16$  pmol/kg (Laukert et al., 2017) which clearly indicate mixing of two water masses, i.e. Atlantic- and Arctic-derived waters. The endmember value of -15 assigned for NAC is slightly less radiogenic compared to the value of North Atlantic Deep water (NADW) -13.5 based on the compilation of Fe-Mn crust from the North Atlantic (Lang et al., 2016; Pena and Goldstein, 2014) which is due to the mixing of Labrador Current (LC) with less radiogenic value ( $\epsilon_{Nd} = -17$ ). However, the maximum influence of LC is restricted up to 2000 m depth as shown in the supplementary Fig. S7b. The major fraction of NADW is primarily comprises of North Atlantic current which shows stable  $\epsilon_{Nd}$  values at around -13.5 for our target interval 3.5 – 2.5 Ma (Lang et al., 2016), therefore, it is expected that the assigned value of NAC ( $-15 \pm 1$ ) would also be constant thought this time interval.

Further, significant glacial-interglacial changes in the erosion input from the Laptev shelf through the Transpolar Drift could contribute to the variability of the PW endmember; however, their variability would be restricted within the reported range from -9.4 to -12.2 with an average of  $-10.8 \pm 2$  (Fagel et al., 2014). Our endmember value assigned for the PW endmember is  $-9.9 \pm 1$  (1SD) is almost similar to the average sediment value of the Laptev shelf. Therefore, changes in the contributions from the Laptev Sea during the glacial-interglacials is expected to have minimal/or negligible impacts as the variability due to such contributions could be accommodate within the uncertainty assigned for the PW endmber i.e.  $\pm 2$  ( $2\sigma$  SD). Another possibility could be variable IRD fluxes from the various sub-basin in the Arctic could have contributed to the PW endmember value. However, several studies from the Arctic including the IRD record from our core ODP 910C shows that IRD fluxes were almost stable during the warmer climate conditions i.e. Holocene (Fagel et al., 2014), interglacials of the Quaternary (Maccali et al., 2013) and Pliocene (Blake-Mizen et al., 2019; Knies et al., 2014). Icebergs and sea ice with incorporated sediments from the Siberian shelf (Kara/Laptev Sea) are exported toward Fram Strait, where they melt when the TPD encounters the warmer Atlantic water resulting in the release of their entrained IRD. Dissolution of these IRD could contribute radiogenic Nd to the Arctic endmembers. However, Nd and Pb coupled isotopes studied in the detrital records from the Yermak Plateau, ODP911 core site (Teschner et al., 2016) demonstrated that possibility of the IRD derived from the Siberian shelf through Transpolar Drift could be ruled out during the low IRD accumulation rates. Further Nd and Pb isotope record show low variability and supports a constant sediment supply prior to iNHGs (~2.7 Ma). Therefore, uncertainty associated with the PW endmember

relatively well constrained prior to iNHGs particularly during our target interval 3.6 – 2.6 Ma. In conclusion, we agree that PW endmember for the glacial periods (M2 and iNHGs) might potentially suffer higher uncertainty due to enhanced IRD flux and weathering inputs associated with higher glacial activity, however, such effects during the mPWP are likely insignificant due to the relatively stable climate and lower IRD fluxes (Blake-Mizen et al., 2019; Knies et al., 2014).

### **S3. Time series analysis to identify frequencies and their evolution**

In order to identify frequencies and their evolution of the proxy records, we performed power spectrum and wavelet analysis. A Fortran 90 program (REDFIT) (Schulz and Mudelsee, 2002) was used to test if peaks in the spectrum of a time series are significant against the red noise background from a first-order autoregressive (AR1) process. The spectrum of an irregularly spaced time series is determined without the need for interpolation by means of the Lomb-Scargle Fourier transform. A Matlab code of this program available online <http://www.geo.uni-bremen.de/geomod/staff/mschulz/#software> was used to determine the significant periodicities against the red noise at different significance level.

The wavelet transform can be used to analyze time series that contain nonstationary power at many different frequencies. We use Morlet wavelet to decompose the time series into time-frequency space which enable us to identify the modes of variability and how those modes changes with time (Grinsted et al., 2004). Statistical significance was determined against a red noise. For analysis of the covariance of two time series we used cross wavelet. This highlights common highest power in two time series (Grinsted et al., 2004). Statistical significance was determined against a red noise. This wavelet

analysis was performed using a Matlab code available online <http://grinsted.github.io/wavelet-coherence>.

**Table S1.** Chronology of the ODP Hole 910C

<b>Age (Ma)</b>	<b>Depth (mbsf)</b>	<b>Sedimentation rate (cm/kyr)</b>	<b>Datum</b>	<b>References</b>
2.438	153.38		MIS 96*	(Lisiecki and Raymo, 2005)
2.510	171.00	24.47	MIS 100 Top	(Lisiecki and Raymo, 2005)
2.540	175.70	15.67	MIS 100 Base	(Lisiecki and Raymo, 2005)
2.565	184.67	35.88	MIS 102*	(Lisiecki and Raymo, 2005)
2.645	204.48	24.76	MIS G2*	(Lisiecki and Raymo, 2005)
2.830	223.00	10.01	"Datum A" modified	(Sato and Kameo, 1996)
3.295	260.40	8.04	MIS M2	(Lisiecki and Raymo, 2005)
3.596	305.00	14.82	Gauss/Gilbert	(Lourens et al., 2005)

MIS = Marine Isotope Stage

\* = age of heaviest  $\delta^{18}\text{O}$  value within respective MIS

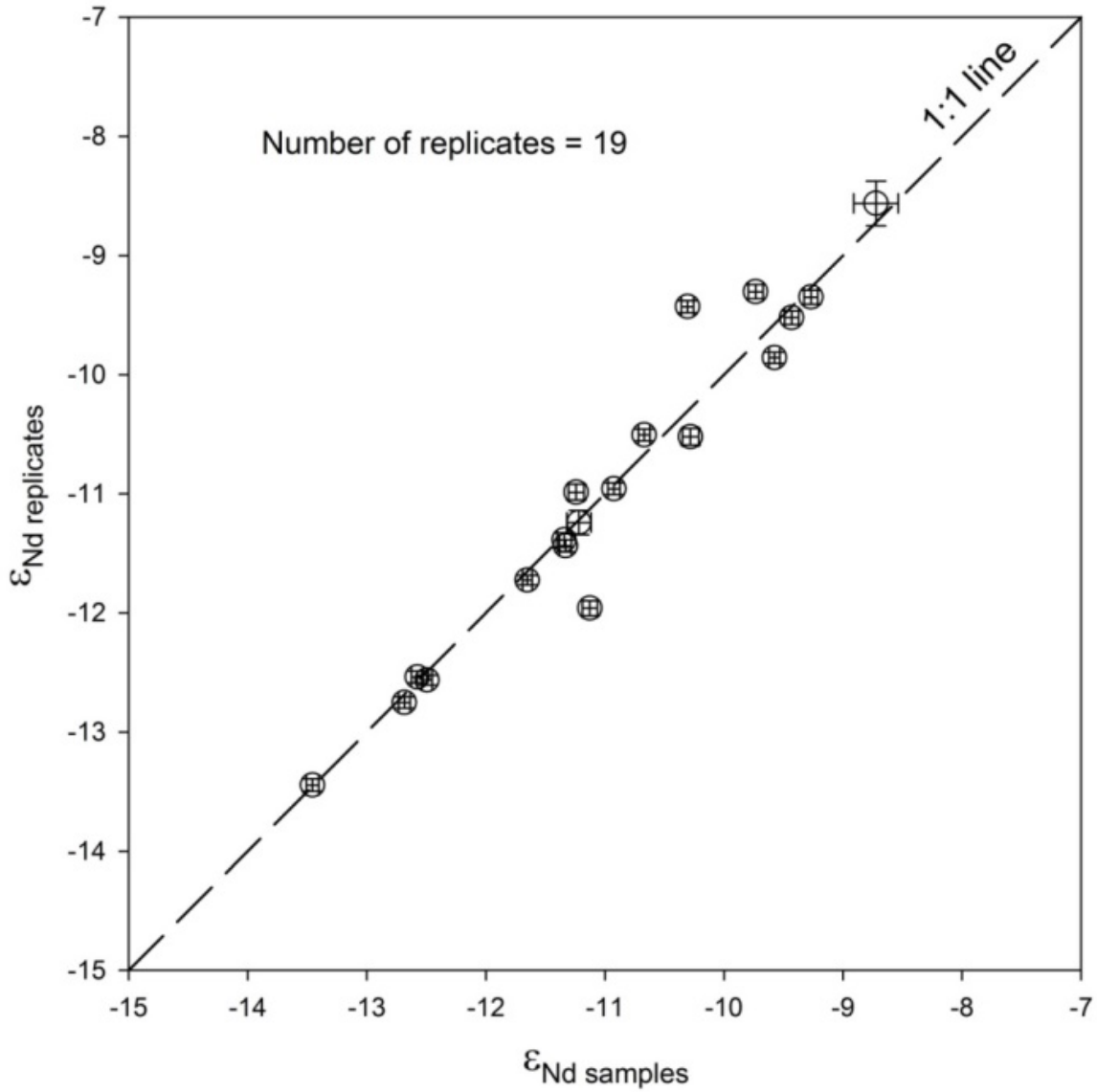


**Fig. S1. Replicate analysis of Nd isotopes in authigenic phases.** To ascertain the quality of the analysis, Nd isotopes were measured in the replicates of the authigenic phases extracted from the bulk sediments of the core samples. A total of 19 replicates were analysed which shows most of the Nd isotope data fall on the equiline (1:1).

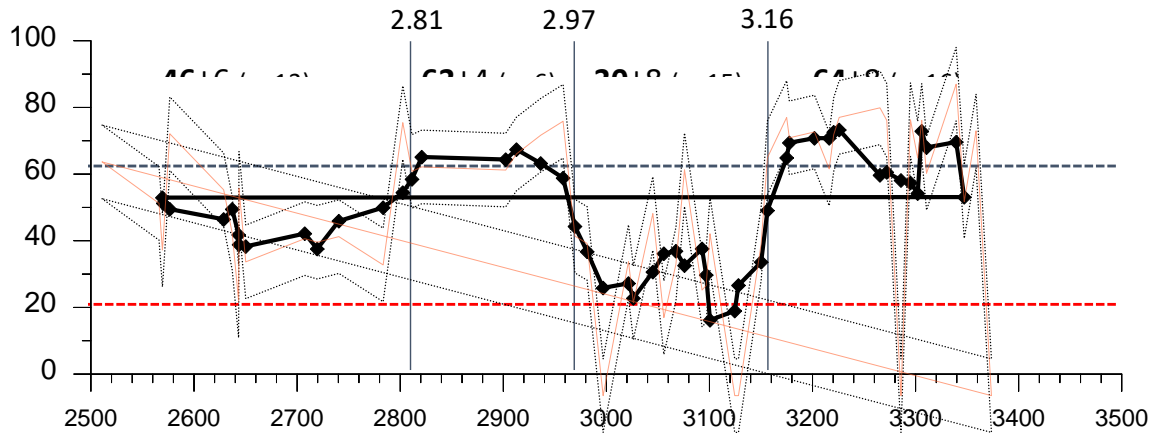


**Fig. S2. Reconstruction of spring sea ice (SpSIC) record.** Plot of spring sea ice (SpSIC) estimates (%) for 910C. Black solid line represents 5-point running mean of the individual SpSIC estimates, which are shown by the solid (thin) red line. The black dotted line in each profile represents RMSE of 11%. Blue and red dashed horizontal lines represent the modern mean (1988-2017, NSIDC) sea ice maximum (62%, Apr-June; spring) and minimum (20%, September; late summer) concentrations at the core site. Summary statistics (**mean**  $\pm$   $\sigma$  (n)) for each section of the record of significant change are shown by black vertical lines.

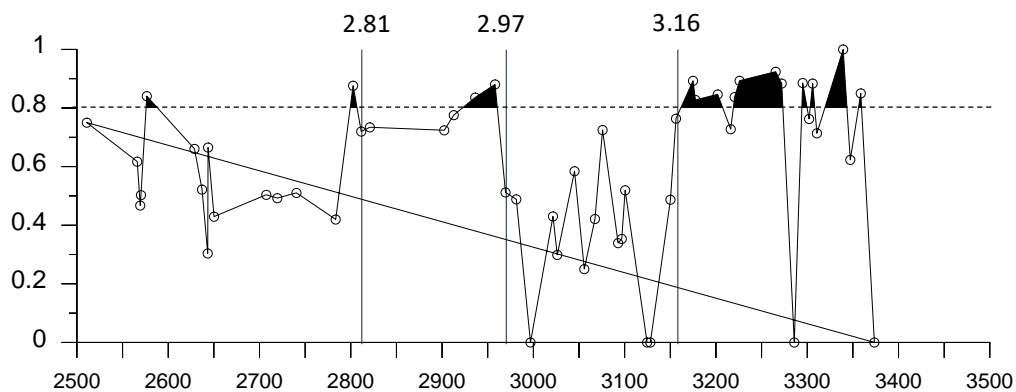


**Fig. S3. Summer and Spring Sea ice records.** Plot of  $P_{IIIIP_{25}}$  values used to derive SpSIC estimates. The horizontal dashed line corresponds to  $P_{IIIIP_{25}} = 0.8$ , a boundary for which the calibration of Smik et al. (2016) showed to be typical of locations with >5% prevailing summer sea ice concentrations (SuSIC).

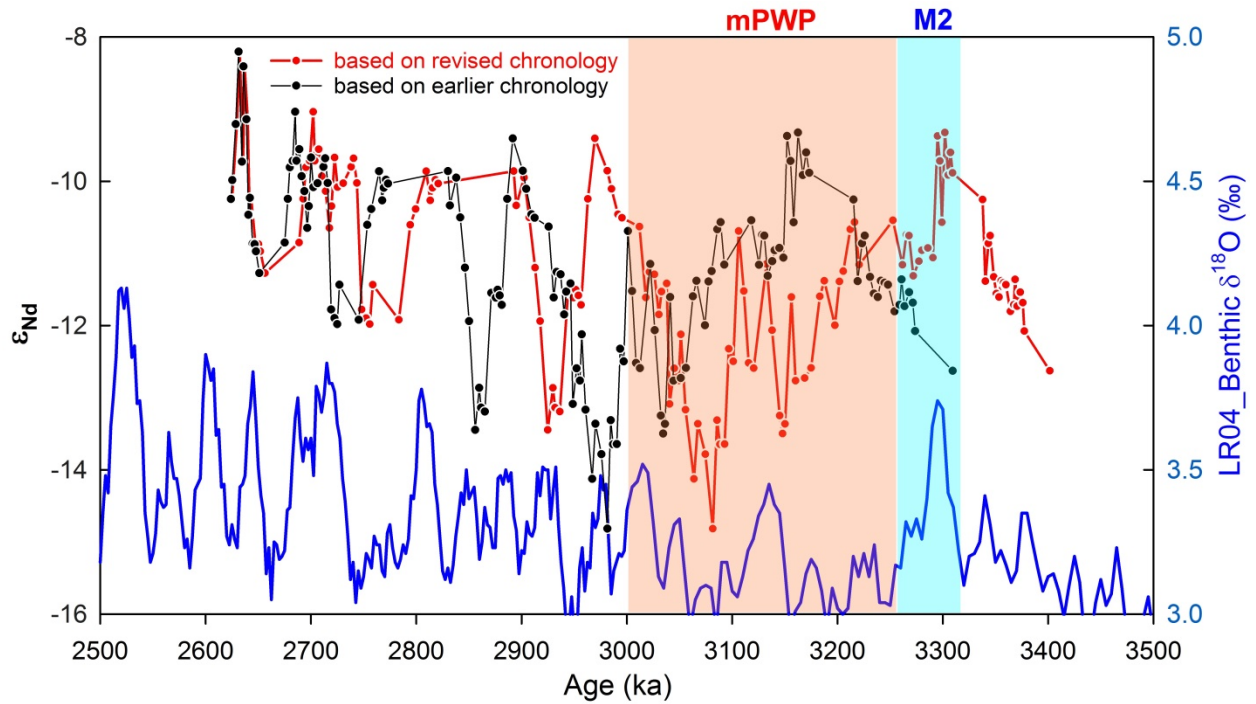


**Fig. S4. Assessment of the chronology.** Comparison of authigenic  $\epsilon_{Nd}$  record from site ODP 910 with global benthic stable oxygen isotope ( $\delta^{18}O$ ) record (LR04 curve(Lisiecki and Raymo, 2005)). The black line with filled circles represents authigenic  $\epsilon_{Nd}$  record based on the earlier published chronology (Knies et al., 2014) whereas the red line with filled circles represents the authigenic  $\epsilon_{Nd}$  record based on the revised chronology in the present study. Based on the revised chronology, the most negative excursion of mPWP in authigenic  $\epsilon_{Nd}$  profile is shifted from 2.981 to 3.081 Ma (older by ~100 ka).



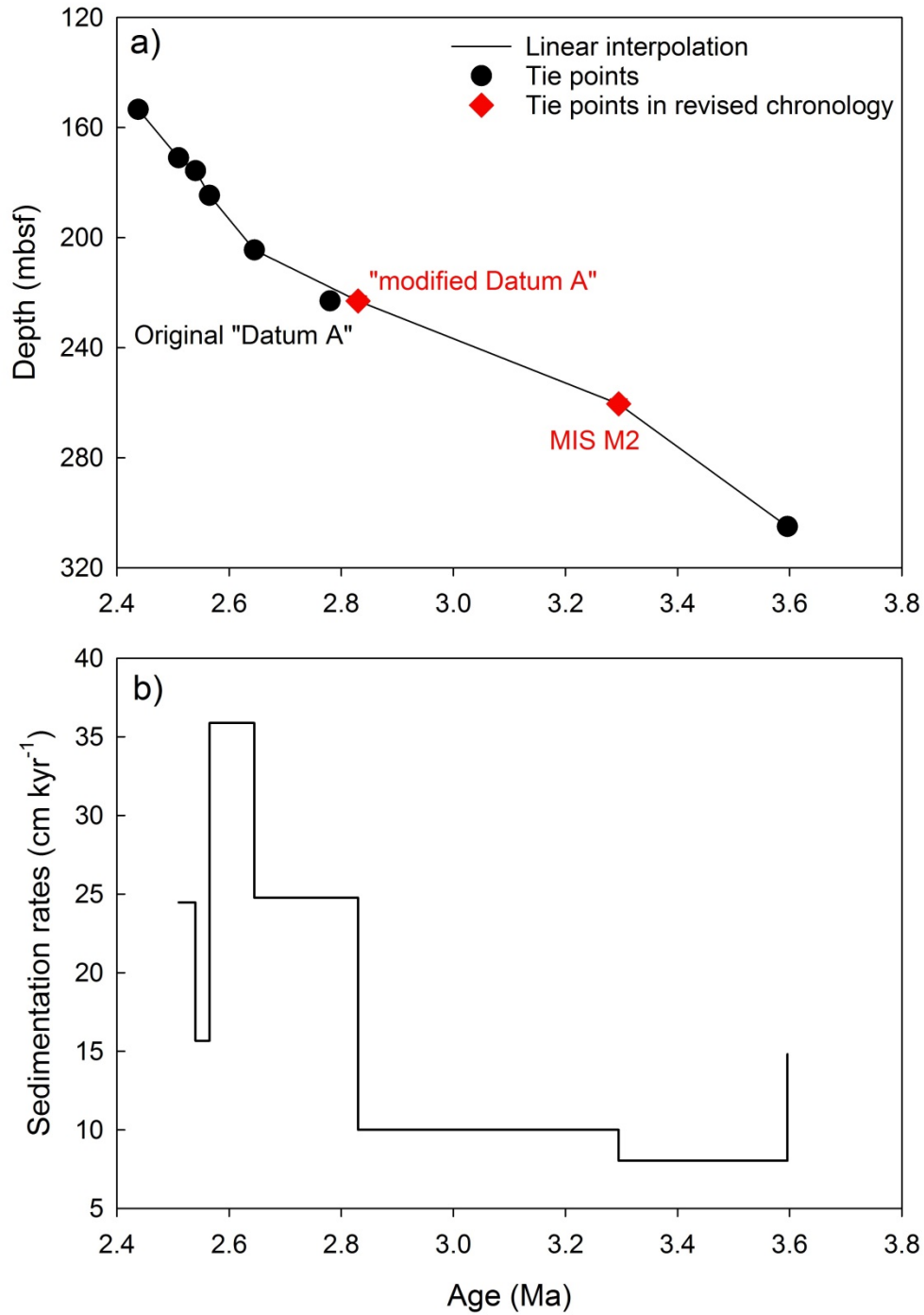


**Fig. S5. Chronology of the ODP 910C core.** (a) Depth versus age. In the revised chronology tie point “Datum A” was slightly modified and a new tie point “MIS M2” was added based on the tuning of LR04  $\delta^{18}\text{O}$  curve and Nd isotope profile as shown in Fig. S4. (b) Sedimentation rates against age.

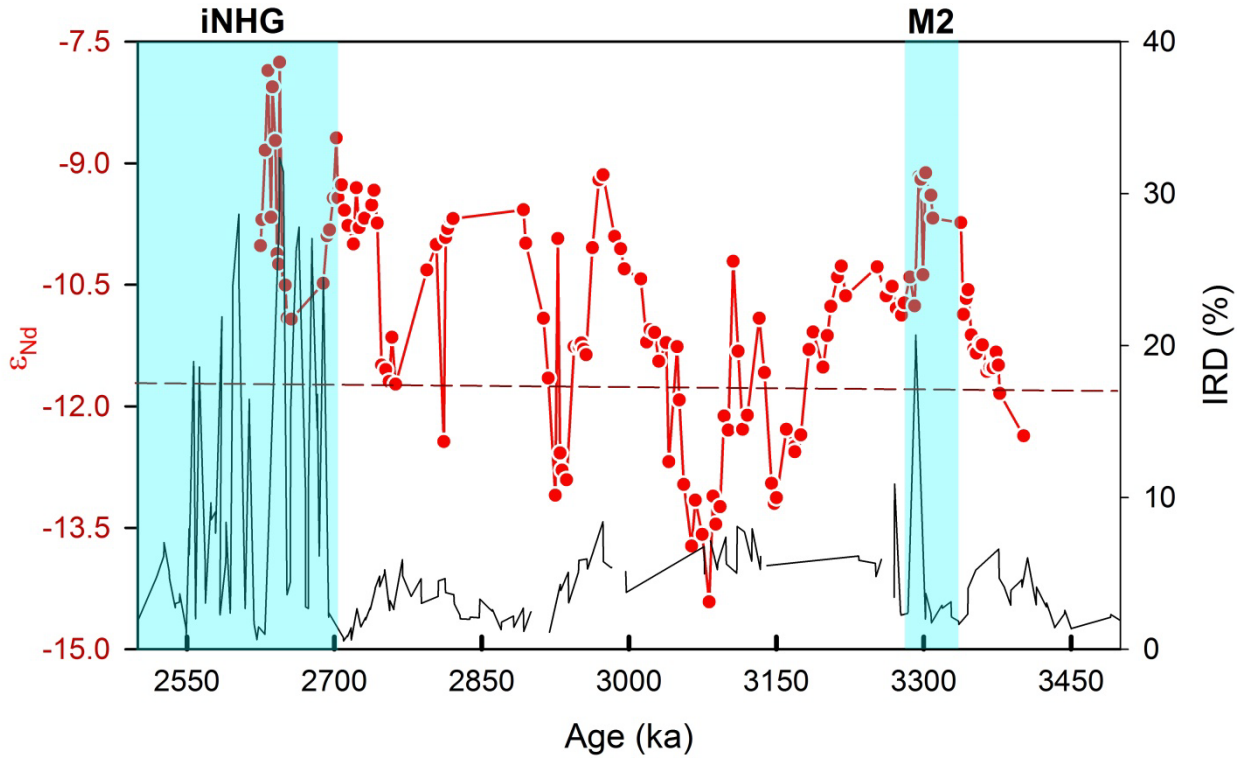


**Fig. S6. Assessing the role of IRD supply on authigenic  $\epsilon_{Nd}$  variability.** Comparison of IRD (Knies et al., 2014) record with authigenic  $\epsilon_{Nd}$  record. Band (cyan colour). Dashed line represents modern water value of  $\epsilon_{Nd}$  at ODP site 911A.

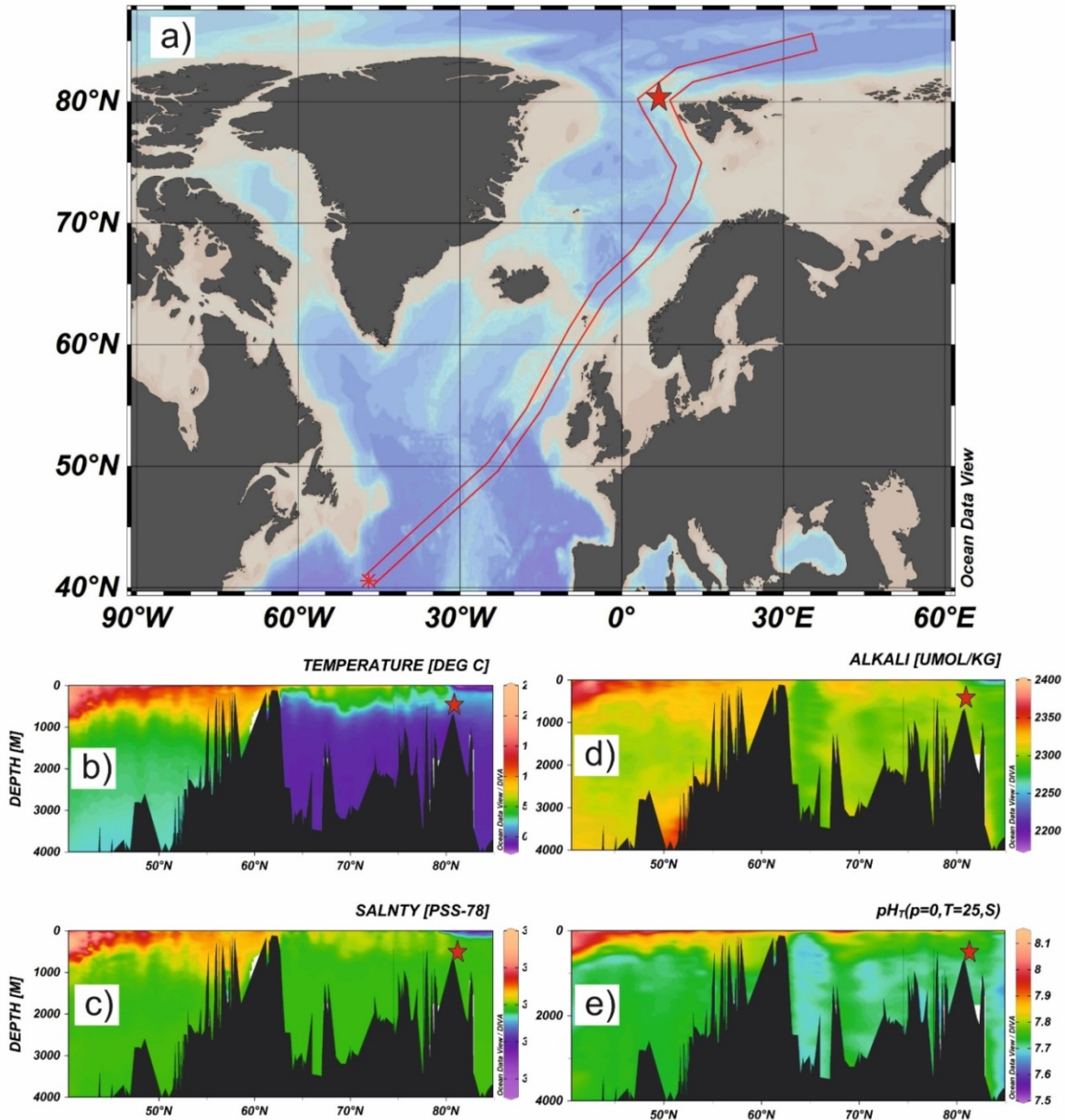


**Fig. S7. Physico-chemical distributions in the Fram-Strait water column.** (a) North-South transect along which physico-chemical parameters are plotted. Section along (red colour rectangle) shows vertical distribution. Distribution of (b) temperature, (c) salinity, (d) alkalinity and (e) pH along a meridional (N-S) transect (along red tramlines) in the North Atlantic (40° – 85° N). Star represents location of the ODP Hole 910C. These figures are prepared using ODV software (<http://odv.awi.de/en/data/ocean/>).

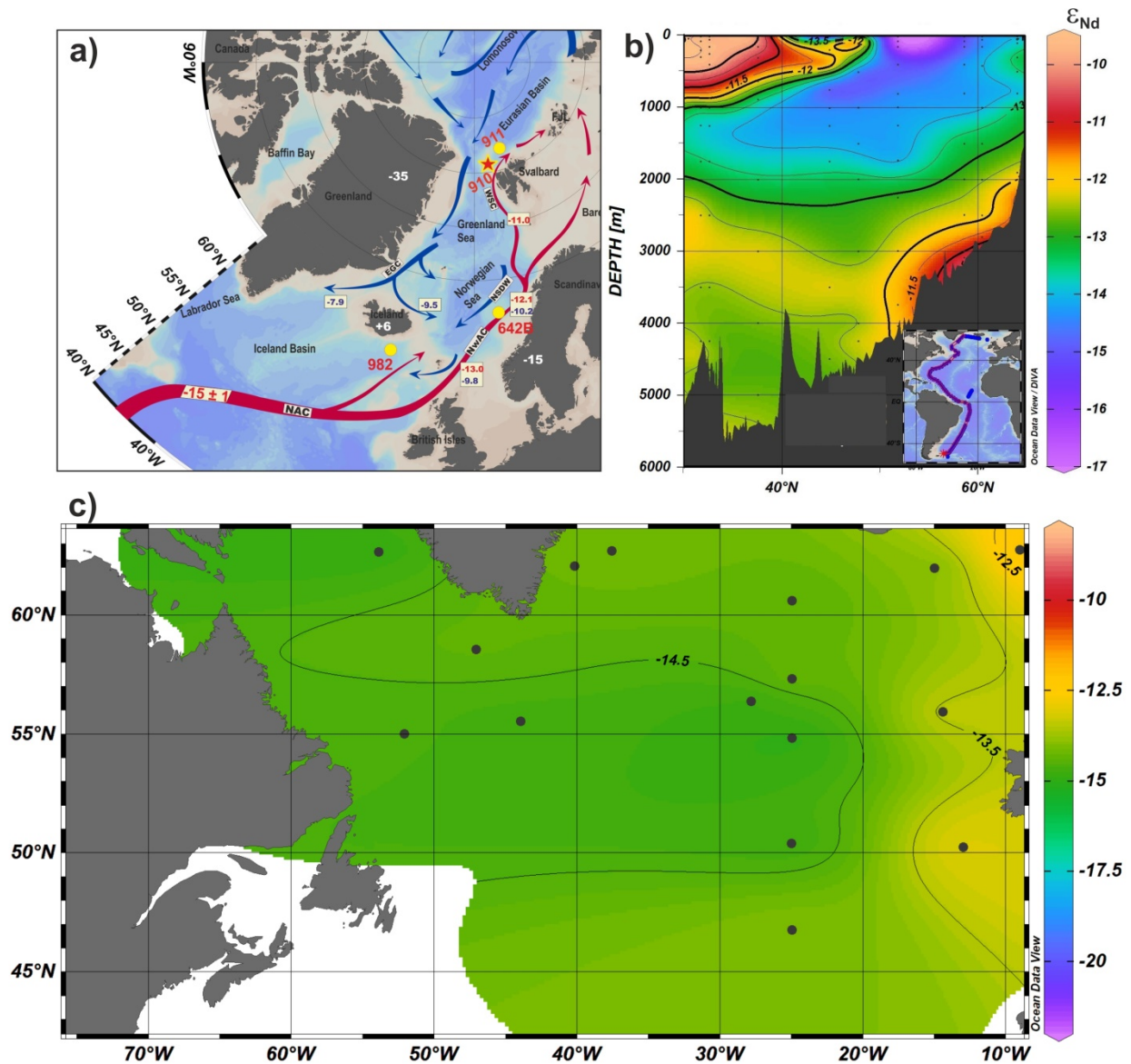


**Fig. S8. Watermass distribution and their characteristic  $\epsilon_{Nd}$  signature.** (a) Map of the North Atlantic and Norwegian-Greenland Seas (Nordic Seas) with locations of ODP Sites 910 (red star) and 911 (filled yellow circle); Schematic flow paths of the main water masses and their present-day  $\epsilon_{Nd}$  signatures are shown (modified from Teschner et al., 2016). Dark red arrows mark the warm inflowing Atlantic water; dark blue arrows represent the cold deep and surface water masses flowing out of the Arctic Ocean, as well as the deep waters in the Norwegian-Greenland Sea (Andersson et al., 2008; François and Catherine, 2004; Lacan and Jeandel, 2004a). White numbers mark the average  $\epsilon_{Nd}$  values of the bedrocks of Svalbard (not shown) (Tütken et al., 2002), Scandinavia and Iceland (Lacan and Jeandel, 2004b), the Putorana basalts in Russia (Sharma et al., 1992) and Greenland. (b) Vertical distribution of water masses on a meridional (N-S) cross-section (along red tramlines) in the North Atlantic characterized by modern  $\epsilon_{Nd}$ . The  $\epsilon_{Nd}$  data was taken from the GEOTRACES GA02 section (Lambelet et



al., 2016). These plots are prepared using ODV software available online (<http://odv.awi.de/>). The  $\epsilon_{Nd}$  value of the NAC near the origin is -15 with an uncertainty of  $\pm 1 \epsilon_{Nd}$  unit (1 SD). c) Spatial distribution of dissolved  $\epsilon_{Nd}$  based on the vertical profile samples within the depths between 200 – 500 m (Dubois-Dauphin et al., 2017).

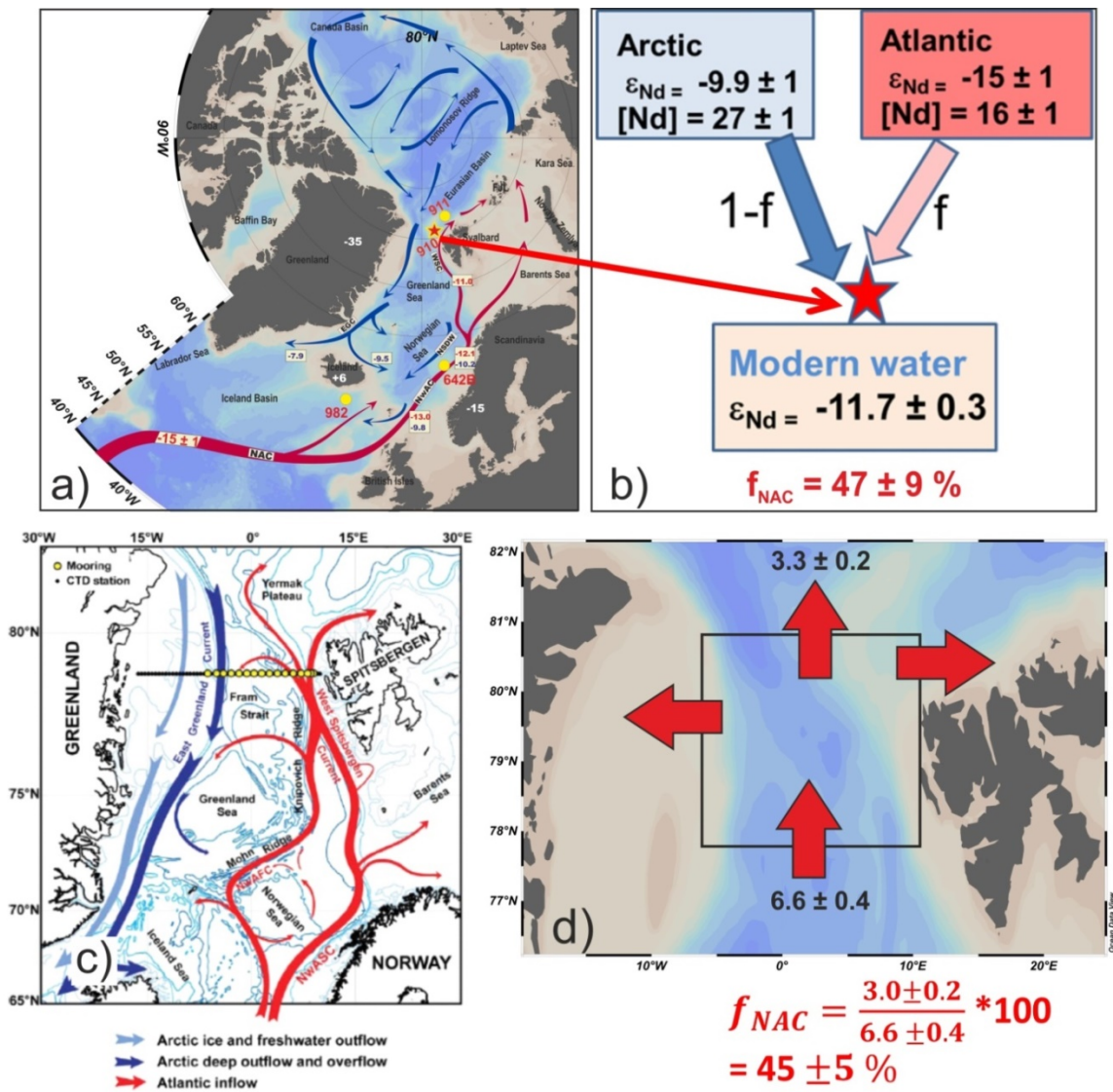


**Fig. S9. Validation of water fraction estimates derived from Nd isotope mass balance.** a) NAC flow with  $\epsilon_{Nd}$  values along the pathway through Fram Strait. Star (red colour) and filled circle (yellow) represent the location of ODP Hole 910C and ODP Hole 911A respectively. b) Binary mixing model based on the Nd isotope mass balance was employed to estimate fractions of water masses i.e. NAC and PW. The estimate of the fraction of NAC based on the modern value of modern  $\epsilon_{Nd}$  at core site is  $47 \pm 9 \%$ . c)

Budget of modern volume transport in the Fram Strait; this is modified from Beszczynska-Møller et al. (2012). This shows a circulation scheme for the Nordic Seas and Fram Strait, showing the locations of the moored array and the annually repeated hydrographic section. The variability in Atlantic water temperature and volume transport in the West Spitsbergen Current (WSC) was estimated based on measurements by an array of moorings in Fram Strait (78°50'N) over the period 1997–2010. The long-term mean net volume transport in the current of  $6.6 \pm 0.4$  Sv (directed northwards) delivered  $3.0 \pm 0.2$  Sv of Atlantic water (NAC) warmer than 2°C ( $1 \text{ Sv} = 10^6 \text{ m}^3/\text{s}$ ). This shows that the fraction of the NAC  $45 \pm 5\%$  of the total northward volume transport.

### Supplementary References

- Andersson, P.S., Porcelli, D., Frank, M., Björk, G., Dahlqvist, R., Gustafsson, Ö., 2008. Neodymium isotopes in seawater from the Barents Sea and Fram Strait Arctic–Atlantic gateways. *Geochimica et Cosmochimica Acta* 72, 2854-2867.
- Beszczynska-Moeller, A., Fahrbach, E., Schauer, U., Hansen, E., 2012. Variability in Atlantic water temperature and transport at the entrance to the Arctic Ocean, 1997-2010.
- Blake-Mizen, K., Hatfield, R., Stoner, J., Carlson, A., Xuan, C., Walczak, M., Lawrence, K., Channell, J., Bailey, I., 2019. Southern Greenland glaciation and Western Boundary Undercurrent evolution recorded on Eirik Drift during the late Pliocene intensification of Northern Hemisphere glaciation. *Quaternary Science Reviews* 209, 40-51.
- Blindheim, J., Østerhus, S., 2005. The Nordic Seas, Main Oceanographic Features.
- Dubois-Dauphin, Q., Colin, C., Bonneau, L., Montagna, P., Wu, Q., Van Rooij, D., Reverdin, G., Douville, E., Thil, F., Waldner, A., Frank, N., 2017. Fingerprinting Northeast Atlantic water masses using neodymium isotopes. *Geochimica et Cosmochimica Acta* 210, 267-288.
- Fagel, N., Not, C., Gueibe, J., Mattielli, N., Bazhenova, E., 2014. Late Quaternary evolution of sediment provenances in the Central Arctic Ocean: mineral assemblage, trace element composition and Nd and Pb isotope fingerprints of detrital fraction from the Northern Mendeleev Ridge. *Quaternary Science Reviews* 92, 140-154.
- François, L., Catherine, J., 2004. Neodymium isotopic composition and rare earth element concentrations in the deep and intermediate Nordic Seas: Constraints on the Iceland Scotland Overflow Water signature. *Geochemistry, Geophysics, Geosystems* 5.
- Grinsted, A., Moore, J.C., Jevrejeva, S., 2004. Application of the cross wavelet transform and wavelet coherence to geophysical time series. *Nonlin. Processes Geophys.* 11, 561-566.

- Knies, J., Cabedo-Sanz, P., Belt, S.T., Baranwal, S., Fietz, S., Rosell-Melé, A., 2014. The emergence of modern sea ice cover in the Arctic Ocean. *Nature Communications* 5, 5608.
- Lacan, F., Jeandel, C., 2004a. Denmark Strait water circulation traced by heterogeneity in neodymium isotopic compositions. *Deep Sea Research Part I: Oceanographic Research Papers* 51, 71-82.
- Lacan, F., Jeandel, C., 2004b. Subpolar Mode Water formation traced by neodymium isotopic composition. *Geophysical Research Letters* 31.
- Lambelet, M., van de Flierdt, T., Crocket, K., Rehkämper, M., Kreissig, K., Coles, B., Rijkenberg, M.J.A., Gerringa, L.J.A., de Baar, H.J.W., Steinfeldt, R., 2016. Neodymium isotopic composition and concentration in the western North Atlantic Ocean: Results from the GEOTRACES GA02 section. *Geochimica et Cosmochimica Acta* 177, 1-29.
- Lang, D.C., Bailey, I., Wilson, P.A., Chalk, T.B., Foster, G.L., Gutjahr, M., 2016. Incursions of southern-sourced water into the deep North Atlantic during late Pliocene glacial intensification. *Nature Geoscience* 9, 375.
- Laukert, G., Frank, M., Bauch, D., Hathorne, E.C., Rabe, B., von Appen, W.-J., Wegner, C., Zieringer, M., Kassens, H., 2017. Ocean circulation and freshwater pathways in the Arctic Mediterranean based on a combined Nd isotope, REE and oxygen isotope section across Fram Strait. *Geochimica et Cosmochimica Acta* 202, 285-309.
- Lisiecki, L.E., Raymo, M.E., 2005. A Pliocene-Pleistocene stack of 57 globally distributed benthic  $\delta^{18}\text{O}$  records. *Paleoceanography* 20.
- Lourens, L.J., Sluijs, A., Kroon, D., Zachos, J.C., Thomas, E., Röhl, U., Bowles, J., Raffi, I., 2005. Astronomical pacing of late Palaeocene to early Eocene global warming events. *Nature* 435, 1083-1087.
- Maccali, J., Hillaire-Marcel, C., Carignan, J., Reisberg, L.C., 2013. Geochemical signatures of sediments documenting Arctic sea-ice and water mass export through Fram Strait since the Last Glacial Maximum. *Quaternary Science Reviews* 64, 136-151.
- Pena, L.D., Goldstein, S.L., 2014. Thermohaline circulation crisis and impacts during the mid-Pleistocene transition. *Science* 345, 318-322.
- Sato, T., Kameo, K., 1996. Pliocene to Quaternary calcareous nannofossil biostratigraphy of the Arctic Ocean, with reference to late Pliocene glaciation. W.F. (Eds.), *Proc. ODP, Sci. Results* 151.
- Schulz, M., Mudelsee, M., 2002. REDFIT: estimating red-noise spectra directly from unevenly spaced paleoclimatic time series. *Computers & Geosciences* 28, 421-426.

- Sharma, M., Basu, A.R., Nesterenko, G.V., 1992. Temporal Sr-, Nd- and Pb-isotopic variations in the Siberian flood basalts: Implications for the plume-source characteristics. *Earth and Planetary Science Letters* 113, 365-381.
- Smik, L., Belt, S.T., Lieser, J.L., Armand, L.K., Leventer, A., 2016. Distributions of highly branched isoprenoid alkenes and other algal lipids in surface waters from East Antarctica: Further insights for biomarker-based paleo sea-ice reconstruction. *Organic Geochemistry* 95, 71-80.
- Teschner, C., Frank, M., Haley, B.A., Knies, J., 2016. Plio-Pleistocene evolution of water mass exchange and erosional input at the Atlantic-Arctic gateway. *Paleoceanography* 31, 582-599.
- Tütken, T., Eisenhauer, A., Wiegand, B., Hansen, B.T., 2002. Glacial–interglacial cycles in Sr and Nd isotopic composition of Arctic marine sediments triggered by the Svalbard/Barents Sea ice sheet. *Marine Geology* 182, 351-372.